TECHNICAL REVIEW

Surface Microphone
NAH and Beamforming using the same Array
SONAH

No.1 2005

Brüel & Kjær

Previously issued numbers of Brüel & Kjær Technical Review

1 – 2004 Beamforming

1 – 2002 A New Design Principle for Triaxial Piezoelectric Accelerometers
Use of FE Models in the Optimisation of Accelerometer Designs
System for Measurement of Microphone Distortion and Linearity from Medium to Very High Levels

1 – 2001 The Influence of Environmental Conditions on the Pressure Sensitivity of Measurement Microphones
Reduction of Heat Conduction Error in Microphone Pressure Reciprocity Calibration
Frequency Response for Measurement Microphones – a Question of Confidence
Measurement of Microphone Random-incidence and Pressure-field Responses and Determination of their Uncertainties

1 – 2000 Non-stationary STSF

1 – 1999 Characteristics of the vold-Kalman Order Tracking Filter

1 – 1998 Danish Primary Laboratory of Acoustics (DPLA) as Part of the National Metrology Organisation
Pressure Reciprocity Calibration – Instrumentation, Results and Uncertainty
MP.EXE, a Calculation Program for Pressure Reciprocity Calibration of Microphones

1 – 1997 A New Design Principle for Triaxial Piezoelectric Accelerometers
A Simple QC Test for Knock Sensors
Torsional Operational Deflection Shapes (TODS) Measurements

2 – 1996 Non-stationary Signal Analysis using Wavelet Transform, Short-time Fourier Transform and Wigner-Ville Distribution

1 – 1996 Calibration Uncertainties & Distortion of Microphones.
Wide Band Intensity Probe. Accelerometer Mounted Resonance Test

2 – 1995 Order Tracking Analysis

1 – 1995 Use of Spatial Transformation of Sound Fields (STSF) Techniques in the Automative Industry

2 – 1994 The use of Impulse Response Function for Modal Parameter Estimation
Complex Modulus and Damping Measurements using Resonant and Non-resonant Methods (Damping Part II)

1 – 1994 Digital Filter Techniques vs. FFT Techniques for Damping Measurements (Damping Part I)

2 – 1990 Optical Filters and their Use with the Type 1302 & Type 1306 Photoacoustic Gas Monitors

1 – 1990 The Brüel & Kjær Photoacoustic Transducer System and its Physical Properties

2 – 1989 STSF — Practical Instrumentation and Application
Digital Filter Analysis: Real-time and Non Real-time Performance

(Continued on cover page 3)

Technical Review

No. 1 – 2005

Contents

TRADEMARKS

Falcon Range is a registered trademark of Brüel & Kjær Sound & Vibration Measurement A/S
PULSE is a trademark of Brüel & Kjær Sound & Vibration Measurement A/S

Editor: Harry K. Zaveri

Acoustical Solutions in the Design of a Measurement Microphone for Surface Mounting

Erling Sandermann Olsen

Abstract

This article describes the challenges encountered, and the solutions found, in the design of surface microphones for measurement of sound pressure on the surfaces of aircraft and cars. Given the microphone's outer dimensions, the optimum rear cavity shape should be found, together with the best possible pressure equalization solution. The microphone's surface should be smooth so as to avoid wind-generated noise. Since the microphones are intended to be used on the surface of aircraft and cars, they must work in a well documented way in a temperature range from –55°C up to +100°C and in a static pressure range from one atmosphere down to one or two tenths of an atmosphere. The static pressure even changes with position on the surface of aircraft and cars due to the aerodynamically generated pressure.

Résumé

Cet article traite des difficultés qu'il a fallu surmonter lors de la conception des microphones de surface utilisés pour les mesures de pression dynamique à la surface des automobiles et des aéronefs, et des solutions qui ont été adoptées. Du fait des cotes extérieures minuscules du microphone, il fallait trouver la forme optimale pour la cavité arrière et la meilleure solution possible pour l'égalisation de pression. Il fallait aussi que la surface soit suffisamment lisse pour éviter tout bruit généré par le vent. Comme ces capteurs sont destinés à des mesures sur les automobiles et les avions, il doivent fonctionner de manière parfaitement documentée dans une gamme de température comprise entre –55°C et +100°C et une gamme de pression statique comprise entre un ou deux dixièmes d'atmosphère et une atmosphère. La pression statique varie par ailleurs en fonction du positionnement sur la surface de l'engin, sous l'effet de la pression aérodynamique.

Zusammenfassung

Dieser Artikel beschreibt Problemstellungen und Lösungen bei der Konstruktion von Oberflächenmikrofonen für Schalldruckmessungen auf der Oberfläche von Flugzeugen und Autos. Bei gegebenen Außenabmessungen des Mikrofons sollte die optimale Form für den rückwärtigen Hohlraum gefunden werden, sowie die am besten geeignete Lösung für die Druckausgleichsöffnung. Die Oberfläche des Mikrofons sollte möglichst glatt sein, um Windgeräusche zu vermeiden. Da die Mikrofone an der Außenfläche von Flugzeugen und Autos eingesetzt werden sollen, müssen sie im Temperaturbereich von −55°C bis +100°C und bei statischen Luftdrücken von 1 atm bis hinab zu 0,1 oder 0,2 atm in dokumentierter Weise arbeiten. Der aerodynamisch erzeugte Druck bewirkt überdies, dass sich der statische Druck mit der Position auf der Oberfläche von Flugzeugen und Autos ändert.

Introduction

At the end of the year 2000, a large-scale aircraft manufacturer approached Brüel & Kjær to find out if we could design and produce a measurement microphone capable of being mounted on aircraft surfaces. At that time, the microphone group in Brüel & Kjær's R&D department was looking at new ways to produce measurement condenser microphones. If successful, this new production technique would allow us to produce the required flat microphone design, and it was therefore decided to carry on with the development. The microphone should be a 5 Hz – 20 kHz pressure field microphone of normal measurement microphone quality, but not more than 2.5 mm in height. It should not interfere with the airflow over aircraft wings and it should work under normal conditions for aircraft surfaces, including large temperature and static pressure variations, de-icing, etc.

Two microphone types have been developed, Brüel & Kjær Surface Microphone Type 4948 and Type 4949. Both are pressure field measurement microphones with built-in preamplifier, 20 mm in diameter and 2.5 mm high. The intention of this article is to present some of the challenges in the acoustic design of the microphones and the solutions to the challenges.

Considerations and Calculations

Influence of Changes in Static Pressure

Changes in the static pressure influence the microphone in two ways:

First, since a part of the stiffness in the diaphragm system of the microphone is due to the mechanical stiffness of the air in the cavity behind the diaphragm, and since the stiffness of the air is proportional to the static pressure [1], the sensitivity depends on the static pressure. The static pressure dependency at low frequencies, expressed in dB/kPa, is given by:

$$S_{\mathrm{ps,dB}} = \frac{d}{dx} 20 \log\left(1 - \frac{c_{\mathrm{d}} \gamma x}{c_{\mathrm{d}} \gamma p_{\mathrm{s}} + V_{\mathrm{c}}}\right) \approx \frac{d}{dx} 20 \log\left(1 - \frac{1}{p_{\mathrm{s}}} \frac{V_{\mathrm{eq,d}} x}{V_{\mathrm{eq,d}} + V_{\mathrm{c}}}\right)$$
$$\approx -8{,}686 \frac{1}{p_{\mathrm{s}}} \frac{V_{\mathrm{eq,d}}}{V_{\mathrm{eq,d}} + V_{\mathrm{c}}} \tag{1}$$

where x is the change in pressure, c_{d} is the mechanical compliance of the diaphragm, γ is the ratio of specific heats of air, p_{s} is static pressure, V_{c} is the volume of the cavity and $V_{\mathrm{eq,d}}$ is the equivalent volume at 1 atmosphere of the diaphragm compliance.

Second, if the static pressure is different outside and inside the microphone, a static force will displace the average position of the diaphragm, and thus change the response of the microphone. Therefore, the cavity must be vented. The vent will have a certain cut-off frequency. Below the cut-off frequency, the microphone is insensitive to pressure variations. Above the cut-off frequency the microphone works as intended. Assuming that the vent is a narrow tube between the cavity and the surroundings and ignoring the influence of heat conduction at the boundaries, the cut-off frequency [1] is given by:

$$f_{\mathrm{NG}} = \frac{1}{2\pi} \frac{c_{\mathrm{d}} + c_{\mathrm{c}}}{R_{\mathrm{v}} c_{\mathrm{d}} c_{\mathrm{c}}} = \frac{1}{2\pi} \frac{\gamma p_{\mathrm{s}} c_{\mathrm{d}} + V_{\mathrm{c}}}{R_{\mathrm{v}} c_{\mathrm{d}} V_{\mathrm{c}}} = \frac{1}{2\pi} \frac{\pi a^4}{8 \eta l} \frac{\gamma p_{\mathrm{s}} c_{\mathrm{d}} + V_{\mathrm{c}}}{c_{\mathrm{d}} V_{\mathrm{c}}} \tag{2}$$

where c_{c} is the mechanical compliance of the cavity, R_{v} is acoustic resistance of the vent, η is the coefficient of viscosity of air and a and l are radius and length of the vent. The dimensions of the tube have to be small. If a cut-off frequency of 5 Hz is desired, the radius must be around 30 μm for the dimensions of the surface microphone.

From the expressions it can be seen that the larger the volume the less dependence on static pressure of the response and the cut-off frequency.

Resonances in the Microphone Cavity

From the previous section, it is clear that the volume of the air cavity must be as large as possible. On the other hand, due to the speed of sound and because the acoustic mass of the air is high in narrow slits [1], resonances will be present if some parts of the volume are too large or too narrow.

In the first prototypes of the microphone all internal volume of the microphone was included in the microphone cavity so as to maximize the cavity volume. All openings between the three internal volumes were as large as possible within the given dimensions. The geometry of the cavity is shown in Fig. 1.

Fig. 1. Sketch of the cross section of the prototype design with maximal internal volume. The maximum internal diameter is approximately 17.5 mm

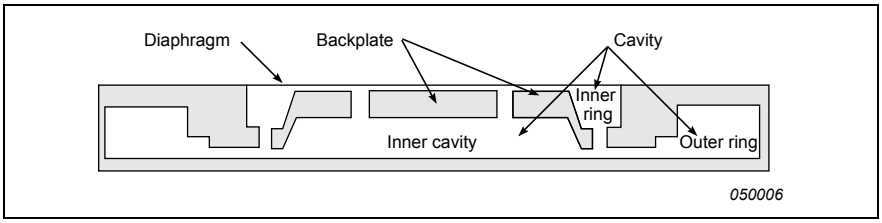

Classical calculations [1] considering the entire cavity and the inner cavity as being simple cylindrical cavities and considering the perimeter length of the ring volumes showed that non-axisymmetrical (cross-sectional) modes could be expected at frequencies down to around 7.5 kHz whereas axisymmetrical modes could be expected at frequencies not lower than 24 kHz. Considering the relatively narrow openings between the internal volumes, Helmholtz-like resonances could be expected. It is difficult to identify exactly what parts of the cavity belong to the mass, but a resonance could be expected in the range 7 kHz to 15 kHz.

Some experiments with the prototype showed that a marked resonance was present at a frequency around 17 kHz, see curve a) in Fig. 4. The dip in the frequency response most probably occurs because a resonance with pressure maximum at the rear of the diaphragm is present. No significant influence of resonances seems to be present at lower frequencies. That is, there was no immediate relation between the estimated resonance frequencies and what was measured. Furthermore, experience from the development of Brüel & Kjær Sound Intensity Calibrator Type 4297 clearly showed that simple acoustical considerations do not necessarily lead to the right conclusions on the acoustics in narrow and complicated cavities [2]. Therefore, it was decided to use an axisymmetrical model for

Boundary Element Model (BEM) calculations of the acoustics in the microphone cavity.

The BEM method used for the calculations was the direct collocation method in a formulation for axisymmetric bodies [3] with an improved calculation method for near-singular integration [4] and using a cosine expansion of the acoustical variables in order to calculate non-axisymmetric sound fields [5]. No losses were taken into consideration in the calculations. Since the condition number of the coefficient matrix of the model presents maxima at eigenfrequencies [6], it was calculated and plotted in order to identify the eigenmodes of the microphone cavity. The method was the same as used for the calculations for Intensity Calibrator Type 4297.

Plots of the condition number as a function of frequency are shown in Fig. 2 for the cavity configurations mentioned in this article. Measured responses for similar configurations are shown in Fig. 4.

Fig. 2. Condition number plots for the first four terms in the cosine expansion of the sound fields in the three cavity configurations mentioned in the text:
a) all three volumes included; b) blocked between inner volume and ring volumes; c) outer ring volume blocked
——: m = 0, axisymmetrical modes *– – – –: m = 1, one nodeline*
· · · · : m = 2, two nodelines *– · – · –: m = 2, three nodelines*

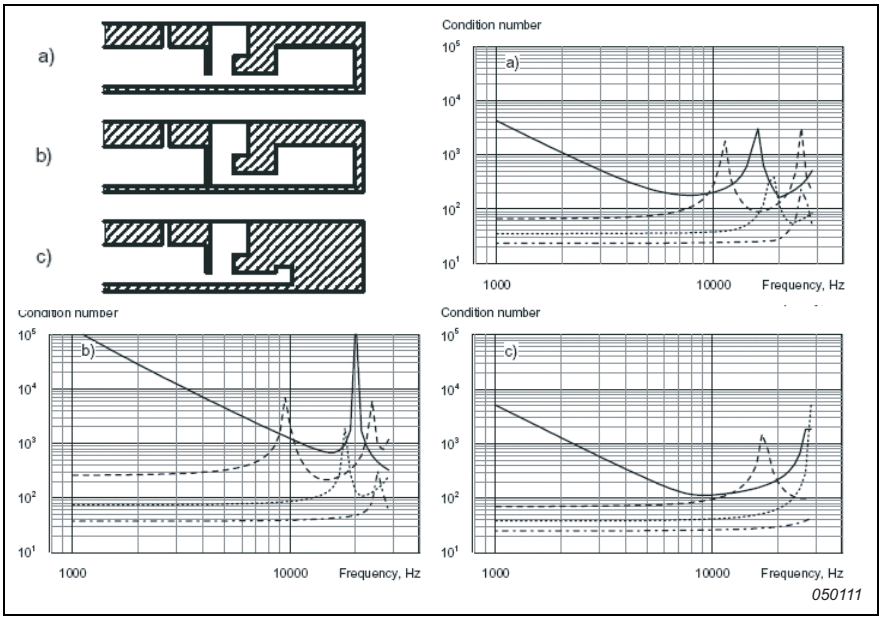

In the first prototype, a) in Fig. 2, a cross-sectional mode is present at around 11.2 KHz and the lowest axisymmetrical mode is present at around 16 kHz. Comparing with the measured response, a) in Fig. 4, the cross sectional mode does not present itself whereas the axisymmetrical mode creates a large dip in the frequency response. The axisymmetrical mode is clearly the expected resonance between the mass of the air in the narrow part and the volumes of the cavity. This can be seen in Fig. 3 where the phase of the sound pressure is shown. The sound pressure in the outer ring is in counterphase with the rest of the sound field in the cavity.

Fig. 3. Phase at 16 kHz of the calculated sound field in the cavity with all three volumes included. The frequency is that of the axisymmetrical mode identified in a) of Fig. 2

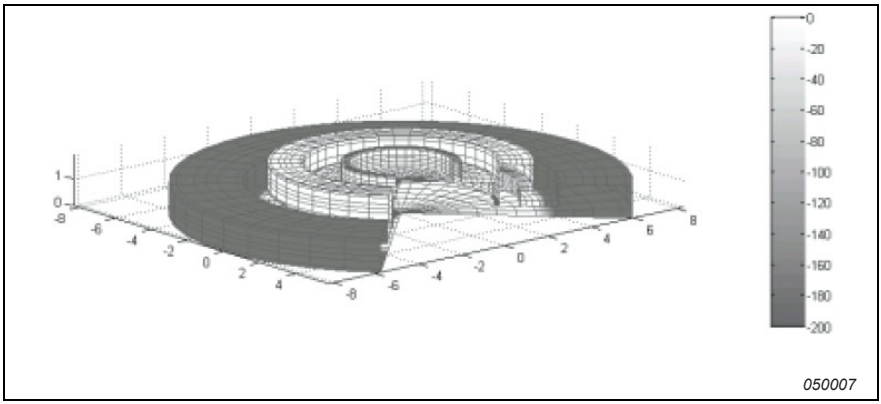

It may be possible to remove the axisymmetrical mode from the frequency range of the microphone without reducing the total cavity volume by blocking the narrow part of the cavity between the inner volume and the ring volumes. The condition numbers are shown for this situation in b) of Fig. 2. As compared to the first example, the lowest cross-sectional mode has moved down in frequency whereas the lowest axisymmetrical mode has moved up in frequency, to just above the microphone's frequency range. This situation is also shown in curve b) in Fig. 4. Although the axisymmetrical eigenmode and thus the dip in the frequency response did move up in frequency, the solution was not found to be satisfactory. This was partly because the frequency of the dip was just outside and not far away from the microphone's frequency range, and partly because blocking at that position would be impractical from a manufacturing point of view.

Reducing the size of the outer ring volume was not an option for practical reasons. Instead, it was decided to block the outer ring volume and to investigate how

Fig. 4. Frequency responses of prototypes with three cavity configurations mentioned in the text: a) all three volumes included; b) blocked between inner volume and ring volumes; c) outer ring volume blocked

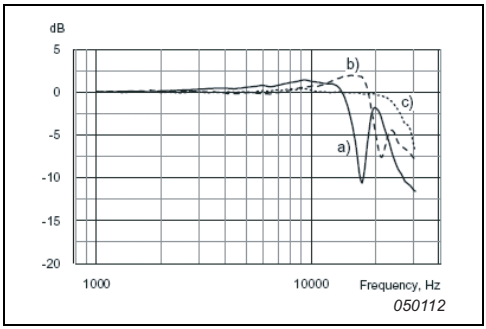

large the active volume could be made without having axisymmetrical modes too close to the microphone's active frequency range. In c) of Fig. 2 condition numbers are shown for a calculation where the narrow part of the gap is blocked on the outside of the openings to the inner ring volume. That is, in these calculations the volume below the backplate and the inner ring volume are coupled through the narrow part of the cavity. Now, the lowest axisymmetrical mode is around 25 kHz, reasonably well above the frequency range of interest. The lowest cross-sectional mode is around 17 kHz. The response of a later prototype with a similar configuration is shown as c) in Fig. 4.

This calculation showed that although the rear cavity had to be substantially smaller than the total internal volume of the microphone, the inner ring volume and some of the narrow sections could still be included in the rear cavity. The resulting volume of the rear cavity is around 90 mm^3. With the equivalent volume of the diaphragm compliance of around 7.5 mm^3, the resulting static pressure dependency of the microphone is around –0.007 dB/kPa. This is within the range normally seen for normal ½″ measurement microphones [7] and it was found acceptable for the microphone. However, if versions of the microphone have to be made with diaphragms with higher compliance, the consequences for the static pressure dependency must of course be considered.

Static Pressure Equalization

As previously mentioned, a narrow tube for venting of the microphone's internal cavity is necessary for the purpose of static pressure equalization. There are some important restrictions to the pressure equalization vent of the microphone – these

form the basis of this article. Since the microphone is intended for surface mounting, the surface which will be mounted flush is likely to be the only part of the microphone housing that is exposed to the same static pressure as the diaphragm. Furthermore, in the presence of airflow, the static pressure can vary over the surface due to aerodynamic lift forces and turbulence. Therefore, the pressure equalization should represent the average static pressure on the surface of the diaphragm as closely as possible.An ingenious pressure equalization solution has been found. A groove is incorporated around the entire diaphragm perimeter and the narrow equalization tube is connected to the bottom of the groove. The pressure equalization system is illustrated in Fig. 5.

Fig. 5. Sketch showing the principle of the static pressure equalization

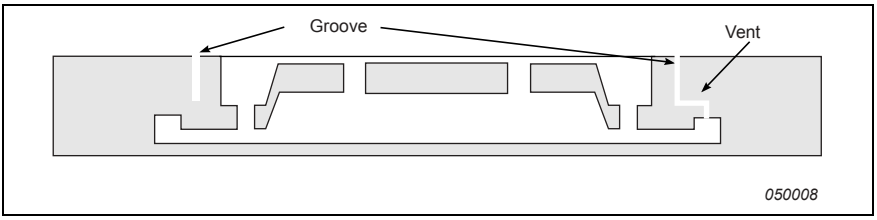

The groove is wide enough to prevent any significant acoustical resistance, and yet it is narrow enough to dampen standing waves and not allow water to penetrate into the groove (under normal circumstances). Of course, in the case of the microphone icing-over, or if the surface of the microphone is temporarily immersed in water, the pressure equalization system will be inoperative, but as long as the groove is open, the equalization system has proven to work as intended in realistic situations as well as in tests.

The pressure equalization solution did present some engineering challenges related to the temperature range of the microphone. Due to changes in properties of the materials in the microphone, it is difficult to maintain contacting surfaces and sealings perfectly airtight at extremely low temperatures, especially because large variations of the dimensions cannot be allowed for in the design. The solution made has proven to work in the specified temperature range. At temperatures below the operating temperature range of the microphone, however, an increase in the lower limiting frequency of the microphone may occur due to minor leakages in the microphone. At least for temperatures the microphone is likely to be exposed to below the temperature range, this is a reversible effect. When the temperature

reverts to within the operating temperature range, the lower limiting frequency reverts to its initial value.

Influence of Airflow

Obviously, a microphone for sound pressure measurements in the presence of rapid airflow must not, by itself, produce any noise due to the airflow. The surface of the microphone must be as flat as possible and have no recesses or obstacles that can generate noise in the presence of the airflow. The surface of the microphone should also be flush with the surface it is mounted in. For applications on aircraft surfaces the microphone must be embedded into the surface, whereas for applications with more moderate wind speeds such as automobile surfaces, the microphone does not necessarily have to be embedded in the surface in order to avoid wind generated noise, as long as there are no sharp edges on the mounting.

The flatness of the microphone is achieved by welding the diaphragm directly on top of its carrying surface. In this way, the diaphragm can be totally flush with the microphone housing. In order to avoid accidental destruction of the diaphragm, however, it is recessed a few hundredths of a millimeter relative to the rest of the surface. The groove for pressure equalization is positioned just outside the welding, so using this method, the microphone is unlikely to have any impact on the airflow.

For applications where the microphone does not have to be embedded in the surface, different mounting flanges have been designed that form a smooth transition from the surface of the microphone to the surrounding surface. These flanges are made slightly flexible so that they can be mounted easily on moderately curved surfaces.

Conclusions

In this article the solutions to some acoustical challenges in the practical design of a special microphone have been presented with special emphasis on the influence of static pressure variations.

Axisymmetrical modes present in the rear cavity of a microphone have a significant impact on its response, whereas non-axisymmetrical modes seem to be less significant. The cavity must be designed so that no axisymmetrical wave patterns are present in the useful frequency range of the microphone.

The solutions for static pressure equalization and minimisation of wind-induced noise have been presented. The combinations of classical calculations, BEM calcu-

lations and common sense considerations have led to a successful design of the microphone for surface mounting.

Acknowledgements

The author wishes to thank all his colleagues at Brüel & Kjær who have participated in the development of the Surface Microphone, especially Niels Eirby, Anders Eriksen, Johan Gramtorp, Jens Ole Gulløv, Bin Liu and Børge Nordstrand of the microphone development department whose combined work has led to the successful design of the Surface Microphone.

References

[1] See, for example, Beranek L.L., "*Acoustics*", Acoust. Soc. Am., Part XIII, Acoustic Elements, (1996).

[2] Olsen E.S., Cutanda V., Gramtorp J., Eriksen A., "*Calculating the Sound Field in an Acoustic Intensity Probe Calibrator – a Practical Utilization of Boundary Element Modeling*", Proceedings of the 8th Internationational Conference on Sound and Vibration, Hong Kong (2001).

[3] Seybert A.F., Soenarko B., Rizzo F.J., Shippy D.J., "*A Special Integral Equation Formulation for Acoustic Radiation and Scattering for Axisymmetric Bodies and Boundary Conditions*", J. Acoust. Soc. Am., **80**, 1241-1247 (1986).

[4] Cutanda V., Juhl P.M., Jacobsen F., "*On the Modeling of Narrow Gaps using the Standard Boundary Element Method"*, J. Acoust. Soc. Am., **109**, 1296-1303 (2001).

[5] Juhl P.M., "*An Axisymmetric Integral Equation Formulation for Free Space Non Axisymmetric Radiation and Scattering of a Known Incident Wave*", J. Sound Vib., **163**, 397-406 (1993).

[6] Bai M.R., "*Study of Acoustic Resonance in Enclosures using Eigenanalysis Based on Boundary Element Methods"*, J. Acoust. Soc. Am., **91**, 2529-2538 (1992).

[7] Brüel & Kjær, "*Microphone Handbook for the Falcon Range® of Microphone Products"*, Brüel & Kjær (1995).

Combined NAH and Beamforming Using the Same Array

J. Hald

Abstract

This article deals with the problem of how to design a microphone array that performs well for measurements using both Nearfield Acoustical Holography (NAH) and Beamforming (BF), as well as how to perform NAH processing on irregular array measurements. NAH typically provides calibrated sound intensity maps, while BF provides unscaled maps. The article also describes a method to perform sound intensity scaling of the BF maps in such a way that area-integration provides a good estimate of the sub-area sound power. Results from a set of loudspeaker measurements are presented.

Résumé

Cet article traite de la difficulté de concevoir une antenne microphonique dédiée tout à la fois aux mesures d'imagerie acoustique par holographie en champ proche (NAH) et beamforming (BF) et au traitement NAH des mesures obtenues au moyen d'antennes de géométrie irrégulière. La technique NAH procure typiquement une cartographie calibrée de l'intensité acoustique tandis que l'approche BF fournit des cartes dépourvues d'échelle. Cet article décrit également une méthode de mise à l'échelle des cartes d'intensité acoustique BF de telle manière que l'intégration surfacique conduise à une juste estimation de la puissance acoustique par élément de surface. Avec une présentation des résultats d'un mesurage réalisé avec un jeu de haut-parleurs.

Zusammenfassung

Dieser Artikel beschäftigt sich mit dem Problem, wie sich ein Mikrofonarray konstruieren lässt, das sich für Messungen mit akustischer Nahfeldholographie (NAH) und Beamforming (BF) eignet, sowie damit, wie sich Messungen mit irregulären Arrays für NAH aufbereiten lassen. NAH liefert in der Regel kalibrierte Schallintensitäts-Kartierungen, während BF nichtskalierte Kartierungen liefert. Der Artikel

beschreibt auch eine Methode zur Skalierung der Schallintensität auf BF-Kartierungen, bei der die Integration über die Fläche eine gute Abschätzung der Teilschallleistungen ergibt. Es werden Ergebnisse von einer Messserie an Lautsprechern vorgestellt.

Introduction

Fig. 1 shows a rough comparison of the resolutions on the source plane – R_{BF} and R_{NAH} – that can be obtained with Beamforming (BF) and with Near-field Acoustical Holography (NAH), respectively.

Fig. 1. Resolution of Holography (NAH) and Beamforming (BF)

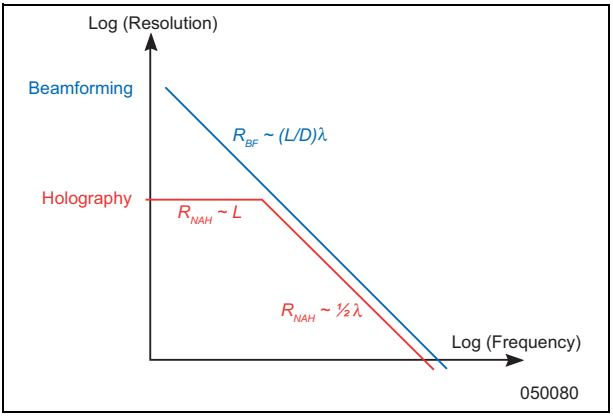

The resolution is defined here as the smallest distance between two incoherent monopoles of equal strength on the source plane that allows them to be separated in a source map produced with the method under consideration. For Beamforming the near-axial resolution is roughly:

$$R_{BF} \approx 1{,}22\frac{L}{D}\lambda \tag{1}$$

where L is the measurement distance, D is the array diameter and λ is the wavelength. (Also see reference [1] and the Appendix.) Basically, Beamforming performs a directional/angular resolution of the source distribution, which explains why the resolution on the source plane is proportional to the measurement distance

L. Since typically, the focusing capabilities of Beamforming require that all array microphones be exposed almost equally to any monopole on the source plane, the measurement distance required is normally equal to, or greater than the array diameter. As a consequence, the resolution cannot be better than one wavelength (approximately), which is often not acceptable at low frequencies.

For NAH, the resolution R_{NAH} is approximately half the wavelength at high frequencies, which is only a bit better than the resolution of Beamforming. But at low frequencies it never gets poorer than approximately the measurement distance L. By measuring very near the source using a measurement grid with a small grid spacing, NAH can reconstruct part of the evanescent waves that decay exponentially away from the source, [2]. This explains the superior low-frequency resolution of NAH.

However, NAH requires a measurement grid with less than half wavelength spacing at the highest frequency of interest, covering at least the full mapping area, to build up a complete local model of the sound field. This requirement makes the method impractical at higher frequencies because too many measurement points are needed. To get a comparable evaluation of the number of measurement points needed for BF we notice that usually the smallest possible measurement distance $L \approx D$ is applied to get the highest spatial resolution. Since further the resolution deteriorates quickly beyond a 30° angle from the array axis, the effective mapping area is only slightly larger than the array area, [1]. Fortunately, by the use of optimised irregular array geometries, good suppression (at least 10 dB) of ghost images can be achieved up to frequencies where the average element spacing is several wavelengths, typically 3–4 wavelengths. So to map a quadratic area with a linear dimension of four wavelengths, NAH requires more than 64 measurement positions, whereas Beamforming can achieve the same results with only one position. This often makes BF the only feasible solution at high frequencies.

A combined measurement technique using NAH at low frequencies and Beamforming at high frequencies therefore seems to provide the best of both worlds. However, traditional NAH requires a regular grid array that completely covers the sound source, while Beamforming provides optimal high-frequency performance with an irregular array that can be smaller than the sound source. The need for repeated change between two different arrays would not be practical, but fortunately the new SONAH (Statistically Optimal NAH) technique for NAH calculations can operate with irregular arrays and it also allows for measurement with arrays smaller than the source, without severe spatial windowing effects, [3].

The principle of the combined measurement technique is illustrated in Fig. 2, using a new so-called 'Sector Wheel Array' design, which will be explained further in the following chapter. Based on two recordings taken with the same array at two different distances (a nearfield SONAH measurement and a BF measurement at an intermediate distance), a high-resolution source map can be obtained over a very wide frequency range. The measurement distance shown for Beamforming is very small – a bit larger than half the array diameter. Simulations and practical measurements described in this article show that with, for example, the irregular Sector Wheel Array of Fig. 2, Beamforming processing works well down to that distance.

Fig. 2. Principle of the combined SONAH and Beamforming technique based on two measurements with the same array

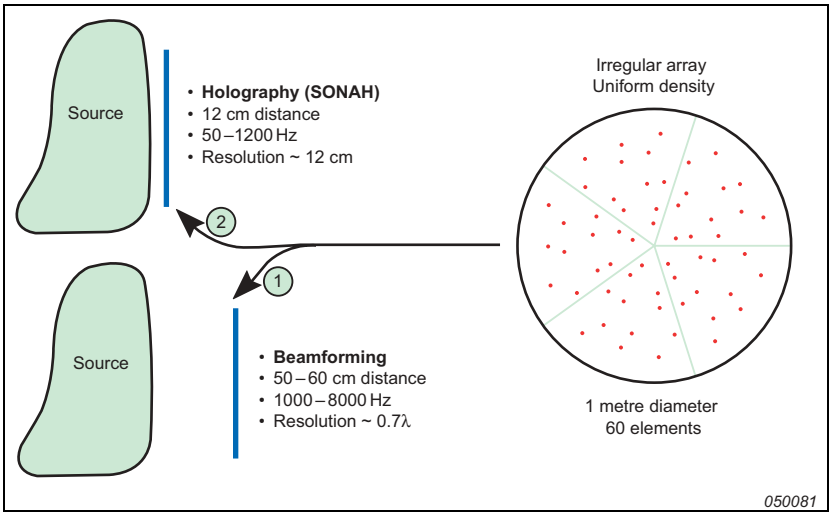

Array Designs for the Combined Measurement Technique

Considering first the Beamforming application, it is well known that irregular arrays provide potentially superior performance in terms of low sidelobe level over a very wide frequency band, i.e., up to frequencies where the average microphone spacing is much larger than half the wavelength, [1]. The best performance is typically achieved, if the set of two-dimensional spatial sampling intervals is non-redundant, i.e., the spacing vectors between all pairs of microphones are different. In references [4] and [1] an optimisation technique was introduced to adjust the

microphone positions in such a way that the Maximum Sidelobe Level (MSL) is minimised over a chosen frequency range. The MSL is defined here on the basis of the so-called Array Pattern, i.e., in connection with a Delay-And-Sum Beamforming method focused at infinite distance, see Appendix and reference [1]. Since typically the MSL has many local minima when seen as a function of the design variables, an iterative optimisation algorithm will usually stop at a local minimum close to the starting point. Many starting points are therefore needed to find a "good solution". Such starting points can, for example, be generated using random number generators to "scan" a certain "space of geometries".
In references [4] and [1] the optimised array geometries were typically *Spoke Wheel Arrays* consisting of an odd number of identical line arrays arranged as spokes in a wheel, see Fig. 3.

Fig. 3. Typical Spoke Wheel Array geometry with 66 microphones optimised for Beamforming applications

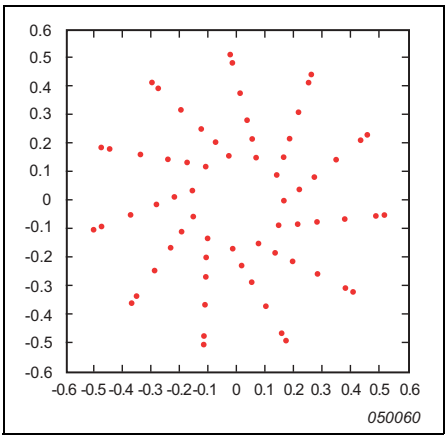

The odd number of spokes is chosen to avoid redundant spatial 2D sampling intervals. The optimisation for low MSL ensures good suppression of ghost images over a wide frequency range, when the array is used at sufficiently long measurement distances, typically down to distances equal to the array diameter. If the distance becomes much smaller than that, the fairly non-uniform density of the microphones across the Spoke Wheel Array area starts to have the effect that different points on the source plane will get very different exposure from the array. In that case, a more uniform density might be better, and numerical simulations have confirmed that hypothesis – specifically for the so-called Sector Wheel Arrays.

When the same array has also to be used for near-field holography measurements at very small measurement distances, a more uniform density is even more important. This will be covered in more detail in the following text.

Various irregular array designs have been published that exhibit a more uniform density of the microphones over the array area and still maintain low sidelobe level over a wide frequency band, for example, the spiral array of [5] and the Packed Logarithmic Spiral array, [6]. These arrays, however, lack the rotational symmetry of the Wheel Array that allows a modular construction and that can be exploited very efficiently in a numerical optimisation to minimise the MSL. Therefore, the Sector Wheel Array geometry was developed. Fig. 4 shows a Packed Logarithmic Spiral array with 60 elements, a Sector Wheel Array with 60 elements and a Sector Wheel Array with 84 elements. For all three arrays the diameter is approximately 1 meter.

Fig. 4. Three different irregular array geometries with uniform element density. The enclosing circle around all three arrays has a diameter of 1.2 meters, so the array diameters are all around 1 meter

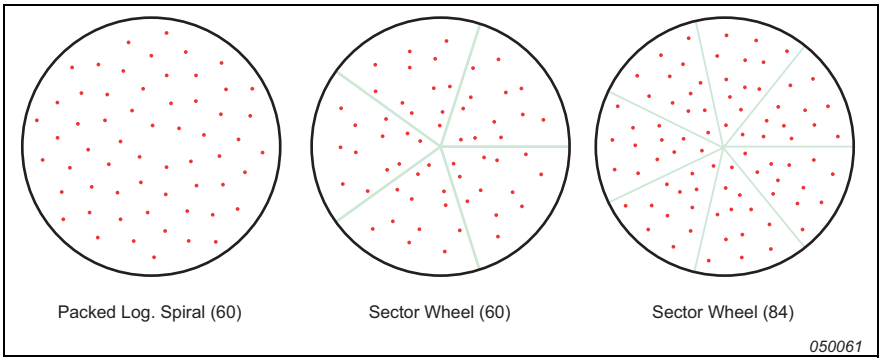

The Sector Wheel Arrays maintain the rotational symmetry of the Spoke Wheel Arrays, but angularly limited sectors replace the small line arrays of the wheel. Each one of the identical sectors contains in this case 12 elements in an irregular pattern, which has been optimised to minimise the MSL of the array.

Fig. 5 shows the Maximum Sidelobe Level (MSL) as a function of frequency for the three array geometries of Fig. 4, and the Spoke Wheel of Fig. 3, assuming focusing of the array to be within 30° from the array axis. If free focusing is required (i.e., up to 90° from the array axis), then the numbers on the frequency axis have to be multiplied by a factor of 0.75, [1]. Clearly, the 84-element array has

very low sidelobe level at frequencies below approximately 2000 Hz, which for free focusing angle would be 1500 Hz. With the array very close to the noise source, as required for holography processing, free focusing angle has to be considered, because waves will be incident from all sides. The 1500 Hz limit turns out to be just a little bit below the frequency, where the average spacing between the elements of the array is half a wavelength. The average element spacing is approximately 10 cm.

Fig. 5. Maximum Sidelobe Level (MSL) for the three different array geometries of Fig. 4 and the Spoke Wheel of Fig. 3. The focusing of the array is restricted here to within 30° from the array axis

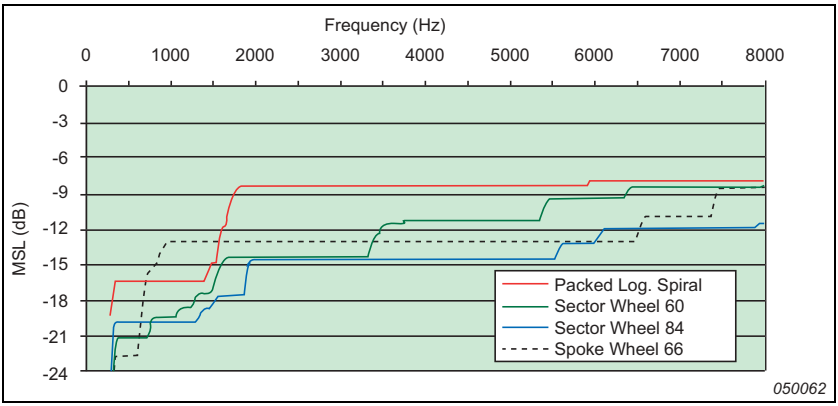

Optimisation of the Sector Wheel Array geometries in Fig. 4 has been performed by adjusting (using a MiniMax optimisation program) the coordinates of the elements in a single sector in such a way that the maximum MSL is minimised over the frequency range of interest. In this process a limit was put on the MSL up to 1500 Hz for the 84-element array and up to 1200 Hz for the 60-element array. As it turned out, this helped maintain the uniform element distribution and therefore the possibility of using the array for holography at frequencies with less than half wavelength average spacing.

The four array designs represented in Fig. 5 will typically be used for Beamforming applications in the frequency range from around 1000 Hz and up to 8000 Hz. Here, the Packed Log Spiral has the highest MSL, which is not surprising since it has not been numerically optimised for minimum MSL. As expected, the 84-channel Sector Wheel has the lowest MSL, since it has been optimised and uses the largest number of elements. The Spoke Wheel array is a bit better than the cor-

responding 60-element Sector Wheel over the Beamforming frequency range. But the Sector Wheel is significantly better over a rather wide range of low frequencies, where it applies for SONAH holography.

Simulation of Beamforming Measurements at a Small Source Distance

Some simulated measurements were performed to investigate how well the three uniform arrays of Fig. 4 would perform with Beamforming from a measurement distance of 0.6 m, i.e., a bit more than half the array diameter. The results are shown in Fig. 6 for the case of 5 uncorrelated monopoles of equal strength at 8000 Hz.

Fig. 6. Simulated measurements on 5 monopoles at 8 kHz and at a measurement distance of 60 cm with the three array designs shown in Fig. 4. The displayed range is 10 dB

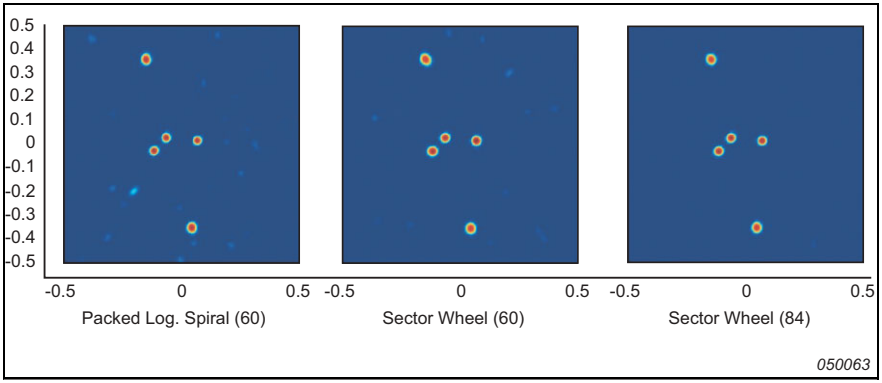

The Beamforming calculations have been performed using the Cross-spectral algorithm (with exclusion of Auto-spectra) described in reference [1], focused on the source plane at 0.6 m distance. Compared to Fig. 5 the Auto-spectral exclusion reduces the MSL by approximately 1 dB at 8000 Hz for the 84-element Sector Wheel and by approximately 0.5 dB for the three other arrays. For all three plots in Fig. 6 the displayed dynamic range is 10 dB, and as expected from Fig. 5, the two 60-element arrays have very comparable performance at 8 kHz with a small advantage to the Sector Wheel Array. The 84-element Sector Wheel Array has 3 dB lower sidelobe level at 8 kHz, and therefore there are no visible ghost images in Fig. 6. The MSL values are seen to be slightly higher at the very short measurement

distance than for the infinite focus distance represented in Fig. 5 – typically around 2 dB higher. The 8 kHz data presented in Fig. 6 are not entirely representative for the relative performance of the three arrays over the full frequency range. If we look instead at 3 kHz, then according to Fig. 4 the 60-element Sector Wheel Array has approximately 6 dB lower sidelobe level than the 60-element Packed Logarithmic Spiral.

The following consideration illustrates the advantage of Beamforming over NAH for source location at high frequencies. If the maps in Fig. 6 had been produced with traditional NAH, then a measurement grid with dimensions around 1.2×1.2 m would have had to have been used, with a grid spacing of around 2 cm – this would have meant approximately 3600 measurement positions!

Numerical Simulations to Clarify the Suitability of the Arrays for Holography

Another series of simulations were performed to investigate the frequency ranges over which the three arrays of Fig. 4 and the Wheel Array of Fig. 3 were suited to SONAH holography measurements. In SONAH (and other types of NAH) a complete reconstruction of the entire near field is attempted over a 3D region around the measurement area. This is possible only if the spatial samples of the sound field taken by the array microphones provide at least a complete reconstruction of the pressure field over the area covered by the array. So from the available spatial samples it must be possible to reconstruct (interpolate) the sound pressure across the measurement area. This can be done by the SONAH algorithm.

The problem of reconstructing a (2D) band-limited signal from irregular samples has been covered quite extensively in the literature; see for example [7]. In order that the reconstruction can be performed in a numerically stable way, it is necessary that the distribution of the sampling (measurement) points exhibit some degree of uniform density across the sampling area. Such a criterion was used in the design of the Sector Wheel Arrays.

For the numerical simulations, a set of (eight) monopole point sources at 30 cm distance from the array was used. All point sources were inside an area of the same size as the arrays. For each frequency and each point source, the complex pressure was calculated at the array microphone positions, and SONAH was then applied to calculate the sound pressure over a dense grid of points inside the measurement area in the measurement plane. For this a 40 dB dynamic range was used, [3]. The interpolated pressure from each monopole was then compared with the known

pressure from the same monopole, and the Relative Average Error was estimated at each frequency as the ratio between a sum of squared errors and a corresponding sum of squared true pressure values. The summation was, in both cases, over all interpolation points and all sources.

Fig. 7 gives a comparison of the Relative Average Interpolation Errors obtained with the four different arrays.

Fig. 7. Comparison of Relative Average Interpolation Error for the three arrays in Fig. 4 and the Wheel Array of Fig. 3. The error is averaged over a set of monopole point sources at a distance of 30 cm

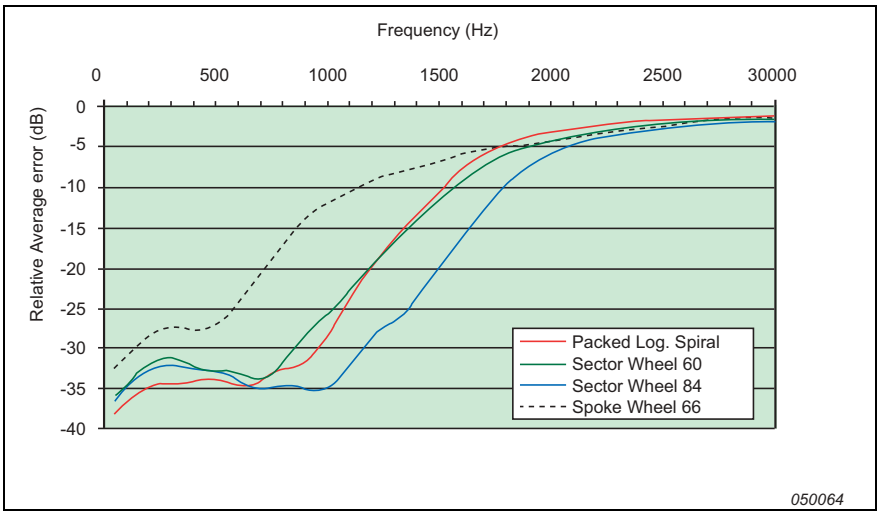

Clearly, the 84-element optimised Sector Wheel Array can represent the sound field over the array area up to the previously mentioned 1500 Hz (approximately), while the 60-element Sector Wheel Array provides acceptable accuracy only up to around 1200 Hz. This actually means that the two Sector Wheel Arrays apply over the same frequency ranges as regular arrays with the same average element spacing. The 60-element Packed Logarithmic Spiral is seen to perform much like the 60-element Sector Wheel Array in connection with SONAH calculations. But as expected, the 66-element Spoke Wheel Array performs much poorer then the three arrays with more uniform element density. The acceptable interpolation accuracy (20 dB suppression of errors) is achieved up to approximately 700 Hz only. If the monopole sources had been positioned nearer the array, this upper frequency would have been even lower.

Intensity Scaling of Beamformer Output

When combining low-frequency results obtained with SONAH and high-frequency results obtained with Beamforming it is desirable to have the results scaled in the same way. This is not straightforward, however, as will be apparent from the following description of the basic output from SONAH and Beamforming.

Based on the measured pressure data, SONAH builds a sound field model valid within a 3D region around the array, and using that model it is possible to map any sound field parameter. Typically the sound intensity normal to the array plane is calculated to get the information about source location and strength. Since the measurement is taken very near the sources, the energy radiated in any direction within a 2π solid angle will be captured and included with the sound intensity and sound power estimates.

Beamforming, on the other hand, is based on a measurement taken at some intermediate distance from the sources where only a fraction of the 2π solid angle is covered by the array. Rather than estimating sound field parameters for the source region, directional filtering is performed on the sound field incident towards the array. As a result only the relative contributions to the sound pressure at the array position from different directions is obtained. Reference [8] describes a scaling of the output that allows the contribution at the array position from specific source areas to be read directly from the Beamformer maps. This is, of course, meaningful only if the pressure distribution across the array area from the various partial sources is fairly constant, which will be true if the array covers a relatively small solid angle as seen from the sources.

But in the context of this article, we wish to take BF measurements as close as possible to the source area, in order to obtain the best possible spatial resolution. As a consequence, the radiation into a rather large fraction of the 2π solid angle is measured. We should therefore be in a better position to get information about (for example) the sound power radiated through the source plane. If we want to scale the Beamformer output in such a way that the scaled map represents the source strength (in some way) it seems logical to scale it as active sound intensity, because that quantity represents the radiation towards the array and into the far-field region. Nearfield pressure contains evanescent components that are not picked up by the array.

The Appendix describes the derivation of a method to scale the output from a Delay-And-Sum Beamformer in such a way that area integration of the scaled output provides a good estimate of the sub-area sound power. For that reason it is natural to use the term “Sound Intensity Scaling” about the method. The derivation is

performed looking at a single monopole point source in the far-field region, and assuming that the array provides a good angular resolution, i.e., assuming the mainlobe covers only a small solid angle. An evaluation is then given of the errors introduced by the far-field assumption and the assumption of a narrow mainlobe. This is done both for Delay-And-Sum processing and for the Cross-spectral algorithm with exclusion of Auto-spectra. The main conclusions are for the 60-element Sector Wheel Array of Fig. 4 and for frequencies above 1200 Hz:

1) The error is less than 0.4 dB when using a measurement distance not smaller than the array diameter.
2) At smaller measurement distances the error increases, but it does not exceed approximately 0.6 dB when the distance is larger than 0.6 times the array diameter.

In the Appendix it is argued that if the scaling works for a single omni-directional source, then it holds also for a set of incoherent monopole sources in the same plane. If sources are partially coherent and/or if single sources are not omni-directional, then because of the limited angular coverage of the array, accurate sound power estimation cannot possibly be obtained. Fortunately, many real-world sound sources tend to have low spatial coherence in the frequency range where Beamforming will be used in the combined NAH/BF method.

The derivation of the scaling is based on matching the area-integrated map with the known sound power for a monopole sound source. In the derivation, area integration was performed only over the hot spot corresponding to the mainlobe of the Beamformer. At high frequencies many sidelobes will typically be within the mapping area, and it turns out that area-integration over a large number of sidelobes will typically contribute significantly to the sound power. This effect can be avoided in practice by the use of a finite dynamic range during the area integration, typically around 10 dB. A frequency dependent adjustment of the integration area to match the resolution is not practical.

The measurement results to be presented in the following section will show the influence of measurement distance, size of the power integration area and of the presence of more than a single source. Also, the sound power estimates will be compared with sound power data obtained from sound intensity maps measured with a sound intensity probe.

Measurements

In order to test the performance of the 60-element Sector Wheel Array of Fig. 4, measurements were taken at 12 cm distance from two small loudspeakers for SONAH processing, and at 55 cm and 100 cm distance for Beamforming processing. The microphones used in the array were Brüel & Kjær Type 4935. At all three distances, measurements were taken with coherent and incoherent white-noise

Fig. 8. 1/3-octave sound intensity maps for the measurements with only the speaker on the right excited by broadband random noise. The four rows represent Beamforming measurements from 100 and 55 cm distance, SONAH from 12 cm distance and measurements with a sound intensity probe at 7 cm distance. The 1/3-octave centre frequencies are shown at the top of the columns. Dynamic range is 15 dB

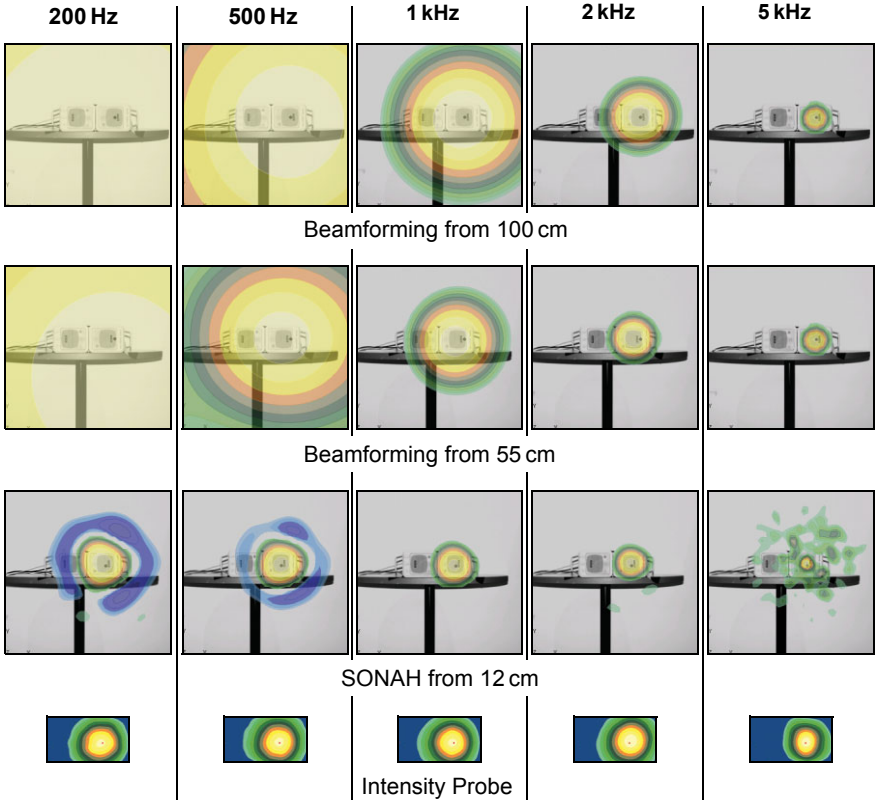

excitation of the two speakers and also with only one speaker excited. For each of these three excitations, a scan was performed approximately 7 cm in front of the two loudspeakers with a Brüel & Kjær sound intensity probe Type 3599. The two speakers were identical small PC units with drivers of diameter 7 cm and they were mounted with 17 cm between the centers of the drivers. The Beamforming processing was performed with the Cross-spectral algorithm with exclusion of Auto-spectra, [1].

Fig. 8 shows 1/3-octave sound intensity maps for the measurements with only the speaker on the right excited. The arrangement of the speaker can be seen in some of the contour plots.

The four rows of contour plots represent the Beamforming measurements taken from a distance of 100 cm and 50 cm, the SONAH measurements taken from 12 cm distance and the measurements taken with an intensity probe from a distance of 7 cm. For the first three rows (representing Beamforming and SONAH results) the sound intensity has been estimated in the source plane over an area of approximate size 80 cm × 80 cm, while the last row shows the sound intensity measured 7 cm from the plane of the speakers over an area of size 36 cm × 21 cm. All plots show a 15 dB dynamic range from the maximum level, with 1.5 dB steps between the colours. Yellow/orange/green colours represent outward intensity and blue colors represent inward intensity. The absolute levels will be presented subsequently through area integrated sound power data.

The resolution obtained with Beamforming and SONAH is in good agreement with the expectations as shown in Fig. 1. The bend on the resolution curve for SONAH is in this case at approximately 1500 Hz, being determined by $\frac{1}{2}\lambda = L$ where L is the measurement distance and λ is the wavelength. Clearly, at low frequencies the Beamforming resolution is very poor, while above approximately 1.5 kHz it is approximately as good as that obtained with the sound intensity probe. SONAH provides good resolution over the entire frequency range, but above approximately 1200 Hz, the average spacing of the microphone grid is too large to reconstruct the sound pressure variation across the measurement area. As a result, distortions will slowly appear as frequency increases, and more evidently – the level will be underestimated as can be seen in the sound power spectra of Fig. 11 and Fig. 12. The combined method using SONAH up to 1250 Hz and Beamforming at higher frequencies provides good resolution at all frequencies, and the sound power estimate is also good as shown in Fig. 11 and Fig. 12. So two recordings taken with the Sector Wheel array at two different distances can provide the information obtained with a time consuming scan with an intensity probe (104 positions

for the small plots in Fig. 8). In addition, many other types of analysis can be performed based on the same data, such as transient analysis of radiation phenomena.

As mentioned previously, the sound intensity scaling of the output from Beamforming is defined in such a way that area integration over the mainlobe area will provide a good estimate of the sound power from a monopole point source. Fig. 9 depicts the 1/3-octave sound power spectra for the single speaker obtained from the

Fig. 9. 1/3-octave sound power spectra for the single speaker measurement. The intensity probe map has been integrated over the entire mapping area shown in Fig. 8. The Beamforming measurement, taken at a distance of 55 cm, has been integrated over the full mapping area and over the mainlobe area only

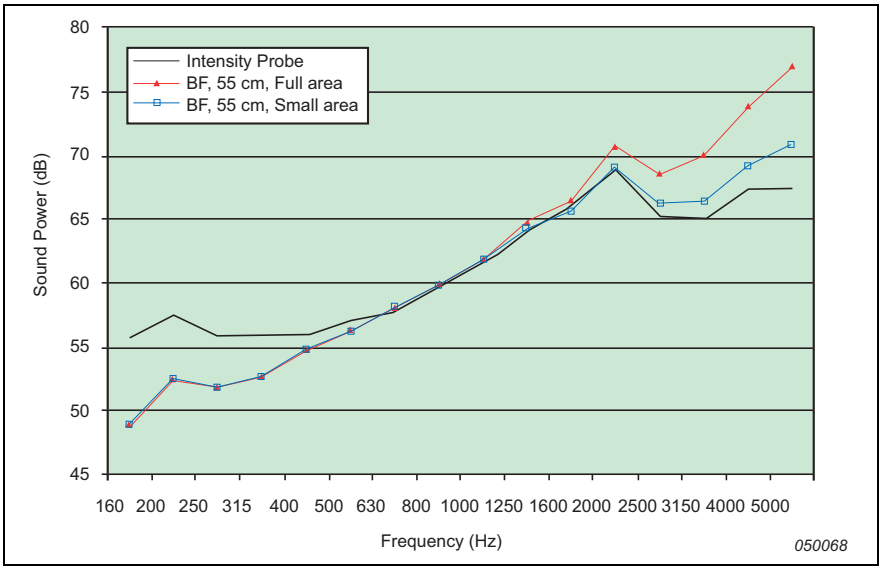

scan with the sound intensity probe and from the Beamforming measurement at 55 cm distance. The intensity probe measurement has been integrated over the full measurement area shown in Fig. 8. Two spectra are shown for the sound power obtained with the Beamforming measurement: one obtained by integration over the full mapping area; another obtained by integration over a small rectangular area with x- and y-dimensions equal to the mainlobe diameter and centered at the known point source position. The radius of the mainlobe is $1.22\lambda L/D$, where λ and L are wavelength and measurement distance (55 cm) as defined above, and where

D is the array diameter of approximately 1 m, refer to equation (A15) in the Appendix. At low frequencies the mainlobe is larger than the entire mapping area of 0.8 m by 0.8 m, and therefore the two Beamforming spectra are identical. Here, the sound power is underestimated, because the power outside the mapping area is not included, and also the assumptions made for the sound intensity scaling fail to hold, refer to the Appendix. At high frequencies the power estimated by Beamforming is too high, even when the integration covers the mainlobe area only. This is mainly because the loudspeaker is no longer omni-directional as assumed in the scaling, but concentrates the radiation in the axial direction, towards the array. At 5 kHz the diameter of the driver unit is approximately one wavelength. Another reason for the over-estimation could be the tendency of the intensity scaling to overestimate when the measurement distance is very small, see Fig. A3. Looking at the sound power obtained by integration over the entire mapping area, it is even higher at the high frequencies. The reason is that sidelobes (ghost images) contribute significantly when the integration area is much larger than the mainlobe area, even when the array has good sidelobe suppression as the present Sector Wheel array.

Fig. 10. 1/3-octave sound power spectra for the single speaker measurement. Again the intensity probe result is included. But now the results from Beamforming measurements at a distance of 55 cm and 100 cm are included. For both of these, the sound power integration covers the entire mapping area

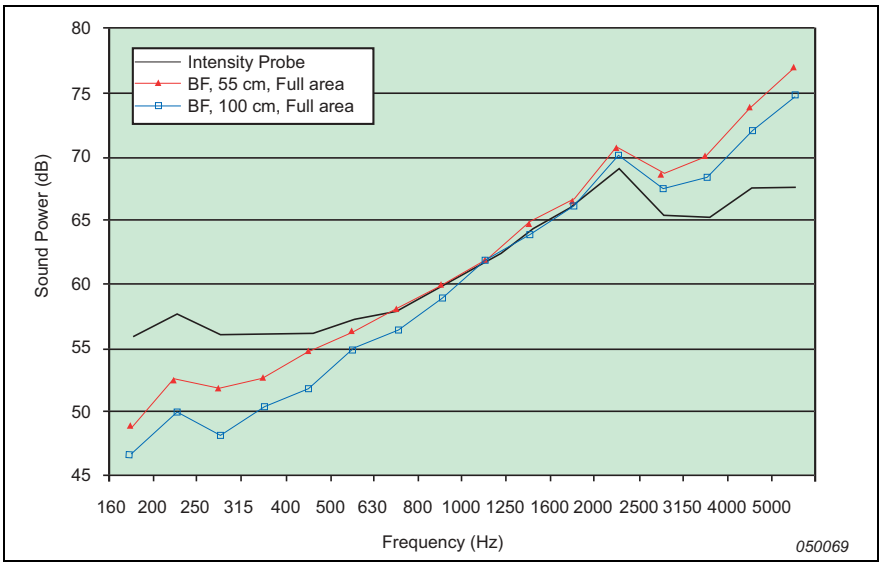

Fig. 10 shows results similar to those of Fig. 9, but instead of focusing on the influence of the size of the power integration area, the influence of the measurement distance is now investigated. For both the Beamforming measurements taken at different distances, the power integration has been performed over the entire mapping area. At low frequencies, the biggest underestimation results from the measurement taken at the longest distance, because the resolution is poorer and consequently a larger part of the power falls outside the mapping area. At high frequencies the measurement at 55 cm distance produces the biggest over-estimation. There are several reasons for that. One is that the sidelobes become a bit stronger at measurement distances smaller than the array diameter. Another reason is the better resolution: a narrower mainlobe means that the ratio between the sidelobe-area and the mainlobe-area increases significantly. Finally, the scaling tends to over-estimate the sound power when used with measurements taken at very small distances, as can be seen in Fig. A3.

Fig. 11 shows the 1/3-octave sound power spectra for the single loudspeaker obtained with intensity probe, SONAH and Beamforming. The Beamforming

Fig. 11. 1/3-octave sound power spectra for the single speaker measurement. The results obtained with Intensity Probe, SONAH and Beamforming are compared

measurement at 55 cm distance has been chosen, and for that measurement the sound power integration has been performed over the full sound intensity map (see Fig. 8), but using only a 10 dB range of intensity data (i.e., data points where the level is less than 10 dB below Peak level are ignored). The result is very close to that obtained with integration over the mainlobe area only, see Fig. 9. Above 500 Hz this leads to a good estimate of the sound power, apart from the previously discussed overestimation at the highest frequencies. SONAH provides good sound power estimates up to approximately 1.6 kHz, apart from a small overestimation (which could be due to the small measurement area that is used with the sound intensity probe). But above 1.6 kHz the sound power is increasingly underestimated with SONAH.

As expected, the results with equal but incoherent excitation of the two speakers are very similar to the results with only one loudspeaker excited. The sound power spectra all increase by approximately 3 dB over the major part of the frequency range, but the differences between the spectra remain unchanged. Therefore no results are shown here.

Fig. 12. 1/3-octave sound power spectra for the case of the two speakers being excited with the same white noise signal. Results obtained with Intensity Probe, SONAH and Beamforming are compared

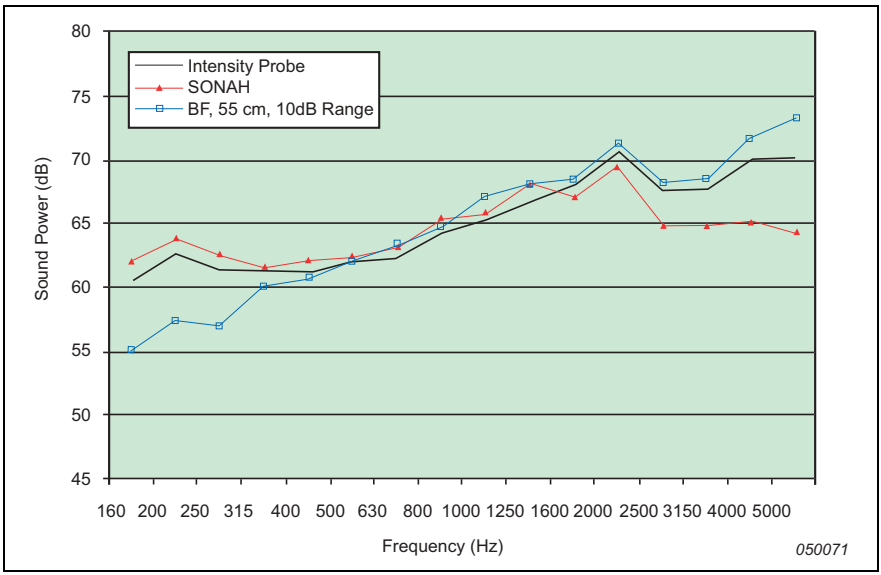

Equal but coherent in-phase excitation of the two loudspeakers will, on the other hand, cause the radiation to deviate more from being omni-directional, which violates the assumptions on which the intensity scaling of Beamformer maps are based.

Fig. 12 depicts the 1/3-octave sound power spectra obtained using intensity probe, SONAH and Beamforming with identical excitation of the two speakers. The SONAH spectrum follows the intensity probe spectrum in much the same way as for the case of only a single speaker being excited. But the sound power obtained from the scaled Beamformer map shows additional deviation in the frequency range from 1 kHz to 2 kHz. In that frequency range the distance between the two speakers is between half a wavelength and one wavelength, which will focus the radiation in the axial direction. But the deviation remains within approximately 2 dB from the power spectrum obtained with the sound intensity probe.

Conclusions

A new combined array measurement technique has been presented that allows Near-field Acoustical Holography and Beamforming to be performed with the same array. This combination can provide high-resolution noise source location over a very broad frequency range based on two recordings with the array at two different distances from the source. The key elements in the presented solution are the use of SONAH for the holography calculation, sound intensity scaling of the Beamformer output and the use of a specially designed irregular array with uniform element density. The optimised Sector Wheel Array is an example of an applicable array with very high performance, particularly for the Beamforming part. Numerical simulations and a set of measurements confirm the strengths of the combined method and of the Sector Wheel array design. The mentioned functionality is all supported in PULSE Version 9.0 from Brüel & Kjær.

Appendix: Sound Intensity Scaling of Beamformer Output

As illustrated in Fig. A1, we consider a planar array of M microphones at locations $\mathbf{r}_m$ ($m = 1,2,...,M$) in the xy-plane of our coordinate system. When such an array is applied to Delay-And-Sum Beamforming, the measured pressure signals p_m are individually weighted and delayed, and then all signals are summed, [9]:

Fig. A1. Illustration of a phased microphone array, a directional sensitivity represented by a mainlobe, and a Plane wave incident from the direction of the mainlobe

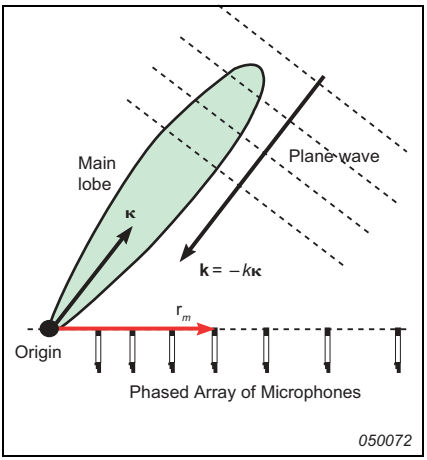

$$b(\boldsymbol{\kappa}, t) = \frac{1}{M} \sum_{m=1}^{M} w_m \, p_m(t - \Delta_m(\boldsymbol{\kappa})) \tag{A.1}$$

The individual time delays Δ_m are chosen with the aim of achieving selective directional sensitivity in a specific direction, characterised here by a unit vector $\boldsymbol{\kappa}$. This objective is met by adjusting the time delays in such a way that signals associated with a plane wave, incident from the direction $\boldsymbol{\kappa}$, will be aligned in time before they are summed. Geometrical considerations (see Fig. A1) show that this can be obtained by choosing:

$$\Delta_m = \frac{\boldsymbol{\kappa} \cdot \mathbf{r}_m}{c} \tag{A.2}$$

where c is the propagation speed of sound. Signals arriving from other far-field directions will not be aligned before the summation, and therefore they will not coherently add up. The 'weights' w_m on the microphone signals are real numbers.

The frequency domain version of expression (A.1) for the Delay-And-Sum beamformer output is:

$$B(\boldsymbol{\kappa}, \omega) = \frac{1}{M} \sum_{m=1}^{M} w_m P_m(\omega) e^{-j\omega\Delta_m(\boldsymbol{\kappa})} = \frac{1}{M} \sum_{m=1}^{M} w_m P_m(\omega) e^{j\mathbf{k}\cdot\mathbf{r}_m} \qquad \text{(A.3)}$$

Here, ω is the temporal angular frequency, $\mathbf{k} \equiv -k\boldsymbol{\kappa}$ is the wave number vector of a fictitious plane wave incident from the direction $\boldsymbol{\kappa}$ in which the array is focused (see Fig. A1) and $k = \omega/c$ is the wave number. In equation (A.3) an implicit time factor equal to $e^{j\omega t}$ is assumed.

Through our choice of time delays $\Delta_m(\boldsymbol{\kappa})$, or the equivalent of the "preferred" wave number vector $\mathbf{k} \equiv -k\boldsymbol{\kappa}$, we have "tuned" the beamformer on the far-field direction $\boldsymbol{\kappa}$. Ideally we would like to measure only signals arriving from that direction, in order to get a perfect localisation of the sound source. To investigate, how much "leakage" we will get from plane waves incident from other directions, we assume now a plane wave incident with a wave number vector $\mathbf{k}_0$ which is different from the preferred $\mathbf{k} \equiv -k\boldsymbol{\kappa}$. The pressure measured by the microphones will then ideally be:

$$P_m(\omega) = P_0 e^{-j\mathbf{k}_0\cdot\mathbf{r}_m} \qquad \text{(A.4)}$$

which according to equation (A.3) will give the following output from the beamformer:

$$B(\boldsymbol{\kappa}, \omega) = \frac{P_0}{M} \sum_{m=1}^{M} w_m e^{j(\mathbf{k}-\mathbf{k}_0)\cdot\mathbf{r}_m} \equiv P_0 W(\mathbf{k}-\mathbf{k}_0) \qquad \text{(A.5)}$$

Here, the function W

$$W(\mathbf{K}) \equiv \frac{1}{M} \sum_{m=1}^{M} w_m e^{j\mathbf{k}\cdot\mathbf{r}_m} \qquad \text{(A.6)}$$

is the so called *Array Pattern*. It has the form of a 2D spatial Fourier transform of a weighting function w, which consists of delta functions at the microphone positions. In the following we will assume all weights w_m to equal one. Because the

microphone positions $\mathbf{r}_m$ have z-coordinates equal to zero, the Array Pattern is independent of K_z. We therefore consider the Array Pattern W only in the (K_x, K_y) plane, and when it is used, as in equation (A.5), the 3D wavenumber vector is projected onto the (K_x, K_y) plane. In that plane, W has an area with high values around the origin with a peak value equal to 1 at $(K_x, K_y) = (0, 0)$.

According to equation (A.5), this peak represents the high sensitivity to plane waves coming from the direction $\boldsymbol{\kappa}$, in which the array is focused. Fig. A1 contains an illustration of that peak, which is called the *mainlobe*. Other directional peaks, which are called *sidelobes*, will cause waves from such directions to leak into the measurement of the mainlobe direction $\boldsymbol{\kappa}$, creating so-called 'ghost sources' or 'ghost images'. The *Maximum Sidelobe Level* (MSL) is defined as the ratio between the highest sidelobe and the mainlobe for a given frequency range.

In the expression (A.5) for the response to a plane wave, notice that the output is exactly equal to the amplitude P_0 of the plane wave, when the array is focused towards the direction of incidence of the plane wave, i.e., when $\mathbf{k} = \mathbf{k}_0$.

For stationary sound fields it is natural to operate with the matrix of cross spectra between the microphones, which provides a better average representation of the stationary phenomena. Exclusion of the auto-spectra offers the possibility of reducing the influence of noise in the individual measurement channels, and it turns out that it also often reduces the sidelobe level, [1]. For the derivation of the sound intensity scaling we will, however, not use the Cross-spectral formulation. But the scaling holds for the Cross-spectral formulation as well, as long as it is scaled in such a way that the response to an in-focus incident plane wave is equal to the squared amplitude of the wave. The formulation in reference [1] is scaled that way. The validity of the intensity scaling in combination with the Cross-spectral Beamformer is investigated both through simulations in this appendix and through the practical measurements.

From the literature it is known that the size and shape of the mainlobe of the array pattern is determined almost entirely by the size and overall shape of the array, [9], [1], while the sidelobes are highly affected by the actual positions of the microphones. The shape of the mainlobe is usually close to the mainlobe from a "continuous aperture" of the same shape as the array or, equivalently, a very densely populated array covering the same area. For circular array geometry, the equivalent continuous aperture has the following array pattern:

$$\overline{W}(K) = 2\frac{J_1\left(\frac{1}{2}KD\right)}{\frac{1}{2}KD}, \qquad K \equiv \left|\tilde{\mathbf{K}}\right| \tag{A.7}$$

where D is the diameter of the aperture (or of the array), J_1 is the Bessel function of order 1, and $\tilde{\mathbf{K}}$ is the projection of $\mathbf{K}$ onto the (K_x, K_y) plane. What we have achieved is a general approximation for the shape of the mainlobe, which is independent of the specific positioning of the microphones,

$$W(\mathbf{K}) \approx \overline{W}(\left|\tilde{\mathbf{K}}\right|) \quad \text{for } \left|\tilde{\mathbf{K}}\right| \le K_1 \tag{A.8}$$

Here, K_1 is the first null of the aperture array pattern, $\overline{W}(K_1) = 0$, given by:

$$\frac{1}{2}K_1 D = \xi_1 \approx 3.83 \tag{A.9}$$

ξ_1 being the first null of the Bessel function of the first order.

Derivation of the Scaling

For the derivation we now assume a single monopole point source on the array axis at a distance L that is so large that the amplitude and phase of the pressure is practically constant across the array area. Thus, for the array the sound field is a plane wave with amplitude P_0 incident with wave number vector $\mathbf{k}_0 = -k\hat{z}$, where $\hat{z}$ is the unit vector in the z-direction. The sound power P_a radiated by the monopole is then:

$$P_a = 4\pi L^2 \cdot I = 4\pi L^2 \cdot \frac{|P_0|^2}{2\rho c} = 2\pi L^2 \cdot \frac{|P_0|^2}{\rho c} \tag{A.10}$$

where I is the sound intensity at the position of the array and ρ is the density of the medium.

The output from the Delay-And-Sum beamformer is according to equation (A.5):

$$B(\boldsymbol{\kappa}) \;=\; P_0 W(\mathbf{k}-\mathbf{k}_0) \;=\; P_0 W(-k\boldsymbol{\kappa}+k\hat{z}) \tag{A.11}$$

where the known values of the two wave number vectors have been inserted. In order to use the approximation (A8) for the mainlobe of the array pattern, we need to project the wave number vectors onto the *xy*-plane, which leads to:

$$B(\boldsymbol{\kappa}) \approx P_0 \overline{W}(k\sin(\theta)) \quad \text{for} \quad |k\sin(\theta)| \le K_1 \tag{A.12}$$

θ being the angle from the array axis (the *z*-axis) to the focus direction $\boldsymbol{\kappa}$.

The Beamformer is now used to create a source map in the plane $z=L$. Each position on this source plane is described by its distance R to the *z*-axis and its azimuth angle ϕ. Assuming relatively small angles from the *z*-axis we can use the approximation:

$$R \;=\; L\tan(\theta) \approx L\sin(\theta) \tag{A.13}$$

where θ is still the angle to the *z*-axis. Use of equation (A.13) in (A.12) leads to the following approximate expression for the "mainlobe" of the beamformed map on the source plane:

$$B(R,\phi) \approx P_0 \overline{W}\left(\frac{kR}{L}\right) \quad \text{for} \quad R \le \frac{K_1 L}{k} \equiv R_1 \tag{A.14}$$

By the use of equation (A.9), we get for the radius R_1 of the mainlobe on the source plane

$$R_1 \equiv \frac{K_1 L}{k} \;=\; \frac{2L}{kD}\xi_1 \approx 1{,}22\frac{L\lambda}{D} \tag{A.15}$$

The scaling factor α needed to obtain the intensity scaled beamformer output,

$$B_I(R,\phi) \equiv \alpha \cdot |B(R,\phi)|^2 \tag{A.16}$$

is now defined in such a way that the integral of $B_I(R, \phi)$ over the mainlobe equals half of the radiated sound power P_a , i.e., the power radiated into the hemisphere containing the array:

$$\frac{1}{2}P_a = \int_0^{R_1}\int_0^{2\pi} \alpha \left|B(R,\phi)\right|^2 R\,dR\,d\phi = 2\pi\alpha\left|P_0\right|^2 \int_0^{R_1} \overline{W}^2\left(\frac{kR}{L}\right) R\,dR \tag{A.17}$$

Use of equation (A.7), substitution with the variable

$$u \equiv \frac{kR}{L}\frac{D}{2} = \frac{kD}{2L}R \tag{A.18}$$

for R in equation (A.17) and application of the relation (A.15) leads to

$$\frac{1}{2}P_a = 2\pi\alpha\left|P_0\right|^2 \int_0^{\xi_1} \left[2\frac{J_1(u)}{u}\right]^2 \left(\frac{2L}{kD}\right)^2 u\,du = \alpha \cdot 32\pi\left(\frac{\left|P_0\right|L}{kD}\right)^2 \cdot \Gamma \tag{A.19}$$

with

$$\Gamma \equiv \int_0^{\xi_1} \left[\frac{J_1(u)}{u}\right]^2 u\,du \approx 0{,}419 \tag{A.20}$$

The scaling factor can finally be obtained through use of the expression (A.10) for the sound power in equation (A.19):

$$\alpha = \frac{1}{32\Gamma}\frac{(kD)^2}{\rho c} \approx \frac{2{,}94}{\rho c}\left(\frac{D}{\lambda}\right)^2 \tag{A.21}$$

Clearly, the scaling factor is proportional to the square of the array diameter measured in wavelengths. This is natural, because the un-scaled beamformer output, with the array focused towards the point source, is basically independent of array

geometry, but the width of the mainlobe is inversely proportional to the array diameter measured in wavelengths (refer to equation A.15). To maintain the area-integrated power with increasing array diameter, the scaling factor must have the proportionality mentioned above.

Evaluation of Errors

The major principle of the scaling is that area integration of the scaled output must provide a good estimate of the sub-area sound power. For that reason it is natural to use the term "Sound Intensity Scaling" about the method. The scaling is defined for a single omni-directional point source in such a way that area integration of the peak created by the mainlobe equals the known radiated power from the point source. So by this definition the total power will be within the mainlobe radius from the source position, and integration over a larger area will cause an overestimation of the sound power. One reason for choosing this definition is that only the mainlobe has a form that depends only on the array diameter and not on all microphone positions. Other choices would be somewhat arbitrary, would require integration over a larger area to get the total power and would need the scaling factor to depend on the particular set of microphone positions. But the influence of the sidelobes on the power integration is a drawback – if the mainlobe is rather narrow and sound power integration is performed over an area much larger than the size of the mainlobe on the source plane, then the level of sidelobes often present in beamforming can contribute significantly to the power integration and cause a significant over-estimation of the sound power. The solution adopted to avoid this significant over-estimation is to use only a finite dynamic range of sound intensity in the area integration, typically around 10 dB. The applied dynamic range, however, should depend on the MSL of the array.

The scaling was derived for a single omni-directional point source on the array axis. Beyond that we have assumed the monopole to be so far away from the array that its sound field has the form of a plane wave across the array. Thus, we have assumed the source to be in the far-field region relative to the array. The second important assumption introduced in equations (A.13 – A.14) above is that the mainlobe covers a relatively small solid angle. To investigate the effect of the last two assumptions, a series of simulations have been performed with the 60-channel Sector Wheel Array of Fig. 4 and with a single monopole point source at different distances on the array axis and operating at different frequencies. The beamforming calculation has been performed with two different beamformers:

1) A Delay-And-Sum beamformer focused at the finite source distance, but without any amplitude/distance compensation, [1].
2) The Cross-spectral beamformer with exclusion of Auto-spectra described in reference [1]. This method compensates for the amplitude variation across the array of the sound pressure from a monopole on the source plane.

The output has then been scaled as sound intensity through multiplication with the scaling factor α of equation (A.21), and finally the sound power has been estimated by integration over a circular area with radius equal to R_1 (refer to equation A.15) around the array axis.

Fig. A2 shows the ratio between the estimated and the true sound power in decibels for the case of the Delay-And-Sum beamformer. At 1000 Hz the mainlobe (and therefore the hot spot generated around the source position on the array axis) covers an angle of approximately 24° from the array axis. This will introduce a significant error in equations (A.13–A.14) and therefore an error in the estimated sound power, even when the source distance is relatively large. Fortunately, SONAH applies below 1200 Hz (approximately) for the particular array, so beamforming will be used typically only above that frequency, and here the error is quite small, provided the measurement distance is not too small. The error increases quickly for distances smaller than approximately 1 m, which is the approximate diameter of the array. Here, the assumption of the source being in the far-field

Fig. A2. Difference in decibels between estimated and true Sound Power. The estimated value is from an Intensity scaled Delay-And-Sum Beamformer. The source is a monopole on the array axis

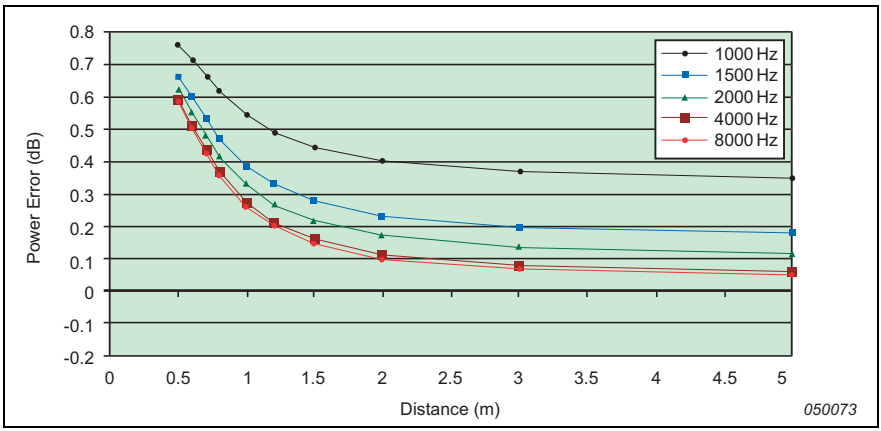

region relative to the array certainly does not hold. But fortunately the error does not get worse than 0.6 dB (approximately) for distances down to half the array diameter. To achieve the best possible resolution it is desirable to use the array at measurement distances as small as this.

Fig. A3 shows the difference between the estimated and the true sound power in decibels for the case of the Cross-spectral beamformer with exclusion of Auto-spectra.

Fig. A3. Difference in decibels between estimated and true Sound Power. The estimated value is from an Intensity scaled Cross-spectral Beamformer with exclusion of Auto-spectra. The source is a monopole on the array axis

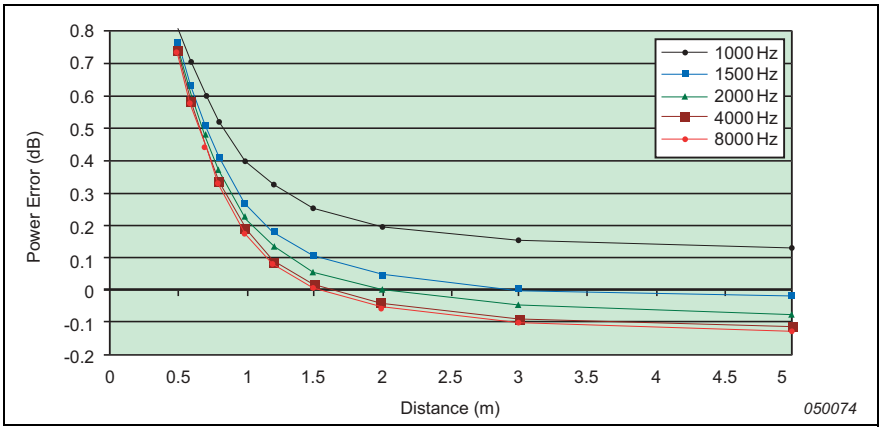

This algorithm is implemented in Brüel & Kjær's Stationary and Quasi-stationary Beamforming calculation software, and therefore it has been used for the measurements presented in this article. Comparison of Fig. 3 and Fig. 4 shows that in general the Cross-spectral algorithm produces smaller errors then the Delay-And-Sum algorithm, except at the very short measurement distance of 0.5 m.

It is, of course, also important to consider, how the sound intensity scaling works for more realistic source distributions than a single monopole. Consider first the case of several omni-directional, but mutually incoherent point sources in the source plane. The incoherent sources will contribute independently to the Cross-spectral matrix between the microphones, i.e., the matrix will be the sum of elementary matrices related to each one of the point sources. If a Cross-spectral Beamformer is used, then the (power) output will equal the sum of contributions from the elementary matrices, meaning that the incoherent partial sources contribute addi-

tively to the Beamformer (power) output. Since they contribute also additively to the Sound Power, the conclusion is that the intensity scaling will hold for a set of incoherent monopole point sources.
When there is full or partial coherence between a set of monopole sources, the radiation from the total set of sources is no longer omni-directional, which will introduce an error that cannot be compensated: The array covers only a certain part of the 2π solid angle for which the sound power is desired. For angles not covered by the array we do not know the radiation and therefore we cannot know the sound power.

References

[1] Christensen J.J., Hald J., "*Beamforming*", Brüel & Kjær Technical Review, No. 1 (2004).

[2] Williams E.G., "*Fourier Acoustics – Sound Radiation and Nearfield Acoustical Holography*", Academic Press (1999).

[3] Hald J., "*Patch Near-field Acoustical Holography using a New Statistically Optimal Method*", Proceedings of Inter-noise 2003.

[4] Hald J., Christensen J.J., "*A Class of Optimal Broadband Phased Array Geometries designed for Easy Construction*", Proceedings of Inter-noise 2002.

[5] Nordborg A., Wedemann J., Willenbrink L., "*Optimum Array Microphone Configuration*", Proceedings of Inter-noise 2000.

[6] Boeringer D.W., "*Phased Array including a Logarithmic Lattice of Uniformly Spaced Radiating and Receiving Elements*", United States Patent US 6,433,754 B1.

[7] Unser M., "*Sampling – 50 Years After Shannon*", Proceedings of the IEEE, Vol. 88, No. 4, April 2000.

[8] Oerlemans S., Sijtsma P., "*Determination of Absolute Levels from Phased Array Measurements Using Spatial Source Coherence*", AIAA 2002-2464.

[9] Johnson D. H., Dudgeon D. E., "*Array Signal Processing: Concepts and Techniques*", Prentice Hall, New Jersey (1993).

Patch Near–field Acoustical Holography Using a New Statistically Optimal Method

J. Hald

Abstract

The spatial FFT processing used in Near-field Acoustical Holography (NAH) makes the method computationally efficient, but it introduces severe spatial windowing effects, unless the measurement area is significantly larger than the source. A Statistically Optimal NAH (SONAH) method is introduced which performs the plane-to-plane calculations directly in the spatial domain. Therefore, the need for a representation in the spatial frequency domain and for zero padding is avoided, significantly reducing the spatial windowing effects. This article describes the SONAH algorithm and presents some results from numerical simulations and practical measurements.

Résumé

Le traitement FFT spatial utilisé dans l'holographie acoustique en champ proche (NAH) rend la méthode efficace sur le plan computationnel mais s'accompagne d'effets de fenêtrage inopportuns, sauf dans le cas où la surface mesurée est significativement plus grande que la source. La méthode faisant intervenir l'algorithme Statistically Optimal NAH (SONAH) est ici présentée. Les calculs étant effectués plan à plan dans le domaine spatial, elle évite le besoin d'une représentation dans le domaine de fréquence spatial et d'un calage du zéro, réduisant de manière significative les effets de fenêtrage spatial. Cet article décrit l'algorithme SONAH et présente plusieurs résultats obtenus par simulation numérique et par mesures pratiques.

Zusammenfassung

Die bei der akustischen Nahfeldholographie (NAH) verwendete räumliche FFT macht die Methode rechnerisch effizient, führt jedoch andererseits zu einem beträchtlichen räumlichen Fenstereffekt, sofern die Messfläche nicht wesentlich größer ist als die Quelle.

Es wird eine statistisch optimierte Methode der akustischen Nahfeldholographie (SONAH) vorgestellt, die Berechnungen von Ebene zu Ebene direkt im räumlichen Bereich ausführt. Damit entfällt die Notwendigkeit für eine Darstellung im räumlichen Frequenzbereich und für Zero Padding, wodurch räumliche Fenstereffekte wesentlich reduziert werden. Dieser Artikel beschreibt den SONAH Algorithmus und stellt Ergebnisse numerischer Simulationen und praktischer Messungen vor.

Introduction

A plane-to-plane propagation of a sound field away from the source can be described mathematically as a 2D spatial convolution with a propagation kernel. A 2D spatial Fourier transform reduces this convolution to a simple multiplication by a transfer function. In Near-field Acoustical Holography (NAH) the Fourier transform is implemented as a spatial FFT of the pressure data measured over a finite area.

The use of spatial FFT and multiplication with a transfer function in the spatial frequency domain is computationally very efficient, but it introduces some errors. The discrete representation in the spatial frequency domain introduces periodic replica in the spatial domain, causing "wrap-around errors" in the calculation plane. A standard way of spacing the replica away from the real measurement area is to use zero padding, introducing, however, a sharp spatial window. Such a window causes spectral leakage in the spatial frequency domain [1]. As a consequence, the measurement area must be significantly larger than the source to avoid very disturbing window effects. This is a problem, for example, in connection with Time Domain NAH, [2], and Real-time NAH, which do not allow the synthesis of a large measurement area through scanning. The new Statistically Optimal NAH (SONAH) method performs the plane-to-plane transformation directly in the spatial domain rather than going via the spatial frequency domain, [3].

Theory of SONAH

The derivation of the SONAH algorithm given in this section is an extension of the derivation given in reference [4]. It is different from, and probably simpler than, the one given in reference [3].

We consider a complex, time-harmonic sound pressure field $p(\mathbf{r}) = p(x, y, z)$ with frequency f and wave number $k = \omega/c = 2\pi/\lambda$ where $\omega = 2\pi f$ is the angular frequency, c is the propagation speed of sound and λ is the wavelength. For the following description we shall assume that the half space $z \geq -d$ is source free and

homogeneous, i.e., the sources of the sound field are for $z < -d$ as shown in Fig. 1. The array measurements are performed in the plane $z = 0$.

Fig. 1. Geometry

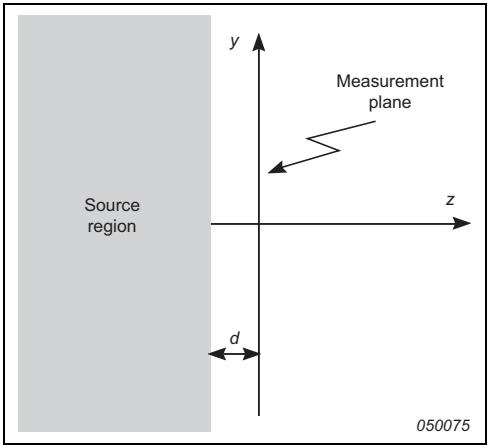

From the theory of NAH, [1], for example, it is well-known that the sound field for $z \geq -d$ can be written as an infinite sum of plane propagating and plane evanescent waves:

$$p(\mathbf{r}) = \frac{1}{(2\pi)^2} \int_{-\infty}^{\infty} \int_{-\infty}^{\infty} P(\mathbf{K}) \Phi_{\mathrm{K}}(\mathbf{r}) d\mathbf{K} \tag{1}$$

Here, $\mathbf{K} \equiv (k_x, k_y)$ is a wave number vector, $P(\mathbf{K})$ is the Plane Wave Spectrum, and:

$$\Phi_{\mathrm{K}}(x, y, z) \equiv e^{-j(k_x x + k_y y + k_z (z+d))} \tag{2}$$

are plane propagating and plane evanescent wave functions.

The z-component k_z of the 3D wave number vector is the following function of $\mathbf{K}$:

$$k_z = k_z(\mathbf{K}) \equiv \begin{cases} \sqrt{k^2 - |\mathbf{K}|^2} & \text{for} \quad |\mathbf{K}| \leq k \\ -j\sqrt{|\mathbf{K}|^2 - k^2} & \text{for} \quad |\mathbf{K}| > k \end{cases} \tag{3}$$

Notice that the elementary wave functions $\Phi_{\mathbf{K}}$ have identical amplitude equal to one on the source plane $z=-d$. The evanescent wave functions outside the Radiation Circle, i.e., for $|\mathbf{K}| > k$, are decaying exponentially away from the source. Since equation (1) has the form of an inverse spatial Fourier transform, the Plane Wave Spectrum P is a representation of the sound field in the spatial frequency domain.

We assume that the complex sound pressure $p(\mathbf{r}_n)$ has been measured at N positions $\mathbf{r}_n \equiv (x_n, y_n, 0)$ on the measurement plane. We wish to estimate the pressure $p(\mathbf{r})$ at an arbitrary position $\mathbf{r} \equiv (x,y,z)$ in the source free region $z \geq -d$, and we wish to estimate $p(\mathbf{r})$ as a linear combination of the measured sound pressure data $p(\mathbf{r}_n)$:

$$p(\mathbf{r}) \approx \sum_{n=1}^{N} c_n(\mathbf{r}) \cdot p(\mathbf{r}_n) \tag{4}$$

In order that equation (4) can provide good estimates for all sound fields with sources for $z \leq -d$, it must in particular provide good estimates for the elementary plane wave functions Φ_{K}. If, on the other hand, equation (4) provides good estimates for all Φ_{K}, then it provides good estimates for any sound field with sources for $z \leq -d$.

We therefore require formula (4) to provide good estimation for a finite sub-set of these elementary wave functions:

$$\Phi_{\mathrm{K}_m}(\mathbf{r}) \approx \sum_{n=1}^{N} c_n(\mathbf{r}) \cdot \Phi_{\mathrm{K}_m}(\mathbf{r}_n), \quad m = 1 \ldots M \tag{5}$$

Solution of this set of linear equations in a 'least squares' sense, for the coefficients c_n, means that we obtain the estimator (4) that is optimal for sound fields containing only the chosen function sub-set, and with approximately equal content of each function, i.e., with equal content of a set of spatial frequencies. Since all functions have amplitude equal to one on the source plane, the estimator is optimised for Plane Wave Spectra P, which are "white" in the source plane.

To solve (5) in a least squares sense we arrange the quantities in matrices and vectors:

$$\mathbf{A} \equiv [\Phi_{\mathrm{K}_m}(\mathbf{r}_n)] \quad \boldsymbol{\alpha}(\mathbf{r}) \equiv [\Phi_{\mathrm{K}_m}(\mathbf{r})] \quad \mathbf{c}(\mathbf{r}) \equiv [c_n(\mathbf{r})] \tag{6}$$

This allows (5) to be written as follows:

$$\boldsymbol{\alpha}(\mathbf{r}) \approx \mathbf{A}\mathbf{c}(\mathbf{r}) \tag{7}$$

The regularised least squares solution to (7) is:

$$\mathbf{c}(\mathbf{r}) = (\mathbf{A}^{\dagger}\mathbf{A} + \theta^2\mathbf{I})^{-1}\mathbf{A}^{\dagger}\boldsymbol{\alpha}(\mathbf{r}) \tag{8}$$

where $\mathbf{A}^{\dagger}$ is the conjugate transpose of $\mathbf{A}$, $\mathbf{I}$ is a unit diagonal matrix and θ is a regularisation parameter. We now let the number M, of elementary wave functions used to determine the estimation coefficients increase towards infinity, and we let the distribution of these wave functions in the $\mathbf{K}$ domain approach a continuous distribution:

$$[\mathbf{A}^{\dagger}\mathbf{A}]_{nn'} = \sum_m \Phi^*_{\mathrm{K}_m}(\mathbf{r}_n)\Phi_{\mathrm{K}_m}(\mathbf{r}_{n'}) \xrightarrow[m\to\infty]{} \frac{1}{\pi k^2}\iint \Phi^*_{\mathrm{K}}(\mathbf{r}_n)\Phi_{\mathrm{K}}(\mathbf{r}_{n'})d\mathbf{K} \tag{9}$$

$$[\mathbf{A}^{\dagger}\boldsymbol{\alpha}]_n = \sum_m \Phi^*_{\mathrm{K}_m}(\mathbf{r}_n)\Phi_{\mathrm{K}_m}(\mathbf{r}) \xrightarrow[m\to\infty]{} \frac{1}{\pi k^2}\iint \Phi^*_{\mathrm{K}}(\mathbf{r}_n)\Phi_{\mathrm{K}}(\mathbf{r})d\mathbf{K} \tag{10}$$

Here, * represents complex conjugate and the integration is over the 2D plane wave spectrum domain. Notice that the switch in equations (9) and (10) to integral representation introduces an identical re-scaling of the matrices $\mathbf{A}^{\dagger}\mathbf{A}$ and $\mathbf{A}^{\dagger}\boldsymbol{\alpha}$. This implies a re-scaling of the regularisation parameter θ of equation (8).

The matrix $\mathbf{A}^{\dagger}\mathbf{A}$ can be seen as an Auto-correlation matrix for the set of measurement positions, while $\mathbf{A}^{\dagger}\boldsymbol{\alpha}$ can be seen as containing cross correlations between the measurement points and the calculation position.

The integrals in equations (9) and (10) can be reduced analytically by conversion of $\mathbf{K}$ to polar co-ordinates: $\mathbf{K} = (k_x, k_y) = (K\cos(\psi), K\sin(\psi))$. We introduce the xy-position vector $\mathbf{R} \equiv (x, y)$ and let $\mathbf{R}_n$ be the xy-component of $\mathbf{r}_n$. From equations (9) and (2) we get:

$$\begin{aligned}[\mathbf{A}^{\dagger}\mathbf{A}]_{nn'} &= \frac{1}{\pi k^2}\iint \Phi^*_{\mathrm{K}}(\mathbf{r}_n)\Phi_{\mathrm{K}}(\mathbf{r}_{n'})d\mathbf{K} \\ &= \frac{1}{\pi k^2}\iint e^{j(k_z^* - k_z)d}\, e^{j\mathbf{K}(\mathbf{R}_n - \mathbf{R}_{n'})}\, d\mathbf{K}\end{aligned} \tag{11}$$

and further by polar angle integration and use of (3):

$$[\mathbf{A}^{\dagger}\mathbf{A}]_{nn'} = \frac{1}{\pi k^2} 2\pi \int_0^{\infty} e^{j(k_z^* - k_z)d} J_0(KR_{nn'}) K dK$$

$$= 2k^{-2} \int_0^{k} J_0(KR_{nn'}) K dK + 2k^{-2} \int_k^{\infty} e^{-2\sqrt{K^2 - k^2}\, d} J_0(KR_{nn'}) K dK \qquad (12)$$

$$= 2\frac{J_1(kR_{nn'})}{kR_{nn'}} + 2k^{-2} \int_k^{\infty} e^{-2\sqrt{K^2 - k^2}\, d} J_0(KR_{nn'}) K dK$$

where $R_{nn'} \equiv \left|\mathbf{R}_n - \mathbf{R}_{n'}\right|$. Equation (10) can be treated in a similar way.

Clearly, all diagonal elements of the Autocorrelation matrix $\mathbf{A}^{\dagger}\mathbf{A}$ are identical because $R_{nn} = 0$ for all n, and the value can be shown to be:

$$[\mathbf{A}^{\dagger}\mathbf{A}]_{nn} = 1 + \frac{1}{2(kd)^2} \qquad (13)$$

To solve for the vector $\mathbf{c}$ of prediction coefficients in equation (8), we need to choose the regularisation parameter θ. It is shown in reference [3] that under some assumptions the optimal value is given by:

$$\theta^2 = \left(1 + \frac{1}{2(kd)^2}\right) \cdot 10^{-\frac{SNR}{10}} \qquad (14)$$

where SNR is the effective Signal-to-Noise-Ratio in Decibels for the microphone signals, taking into account all sources of error.

We can now estimate the pressure at the position $\mathbf{r}$ through use of equation (4):

$$p(\mathbf{r}) \approx \sum_{n=1}^{N} c_n(\mathbf{r}) \cdot \mathbf{p}(\mathbf{r}_n) = \mathbf{p}^{\mathrm{T}} \boldsymbol{c}(\mathbf{r}) = \mathbf{p}^{\mathrm{T}} (\mathbf{A}^{\dagger}\mathbf{A} + \theta^2 \mathbf{I})^{-1} \mathbf{A}^{\dagger} \boldsymbol{\alpha}(\mathbf{r}) \qquad (15)$$

Here, $\mathbf{p}$ is a vector containing the measured pressure signals, and we have used equation (8). Notice that the vector $\mathbf{p}^{\mathrm{T}}(\mathbf{A}^{\dagger}\mathbf{A}+\theta^2\mathbf{I})^{-1}$ of de-correlated pressure data over the microphone positions needs to be calculated only one time. After that it can be used for calculation of the pressure at many other positions $\mathbf{r}$ using other cross correlation vectors $\mathbf{A}^{\dagger}\boldsymbol{\alpha}(\mathbf{r})$.

The particle velocity can be obtained in the same way as a linear combination of the measured pressure signals. To derive the required estimation coefficients we start with an equation equivalent to (5), but with the particle velocity of the elementary wave functions on the left-hand side. As a result, we obtain the following expression for the particle velocity:

$$u_z(\mathbf{r}) \approx \mathbf{p}^{\mathrm{T}}(\mathbf{A}^{\dagger}\mathbf{A} + \theta^2\mathbf{I})^{-1}\mathbf{A}^{\dagger}\boldsymbol{\beta}(\mathbf{r}) \tag{16}$$

where $\mathbf{A}^{\dagger}\boldsymbol{\beta}$ is a vector of correlations between the pressure at the microphone positions and the particle velocity at the calculation position. Notice that the vector $\mathbf{p}^{\mathrm{T}}(\mathbf{A}^{\dagger}\mathbf{A}+\theta^2\mathbf{I})^{-1}$ of de-correlated measured pressure data from equation (15) applies also in equation (16).

Based on the sound pressure and the particle velocity, the sound intensity can be calculated.

Numerical Simulations

A set of measurements was simulated with the set-up illustrated in Fig. 2.

The grid represents an 8×8 element microphone array with 3 cm grid spacing, the microphones being at the corners of the grid. Two coherent in-phase monopole point sources of equal strength are positioned 6 cm below the array, i.e., at a distance that is twice the grid spacing. The positions of the point sources are indicated in Fig. 2 by black dots. Clearly, the array does not cover the entire source area, so NAH will introduce severe spatial window effects. SONAH calculations were performed in the measurement plane ($z = 0$) and in a plane half way between the source plane and the measurement plane ($z = -3$cm). The calculation grid had the same geometry as the measurement grid. The regularisation parameter in equation (8) was set according to an SNR equal to 40 dB, and the source distance d was set to 6 cm.

First, the accuracy of the particle velocity estimation was investigated. For this, the central and the peripheral sections of the calculation area were considered separately, the peripheral section covering the 28 grid positions along the edges, and the

Fig. 2. Microphone grid and point sources. The grid spacing is 3 cm and the two coherent point sources are 6 cm below the array. The left source is 6 cm to the left of the array

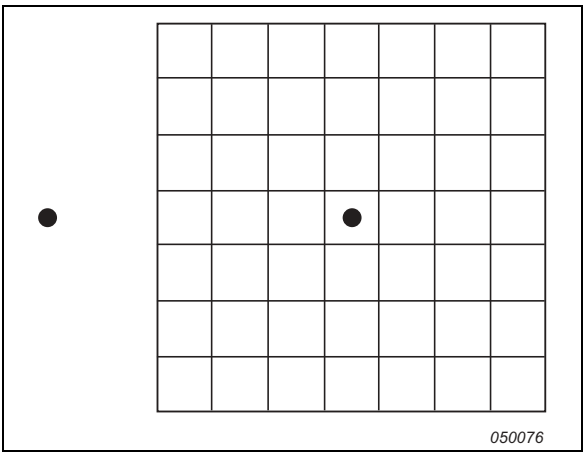

central section covering the rest. For each section/area the relative average error level was calculated from the formula:

$$L_{err} = 10 \cdot \log_{10}\left(\frac{\sum\left|u_i^{true} - u_i\right|^2}{\sum\left|u_i^{true}\right|^2}\right) \tag{17}$$

where the summations are both over the relevant section. A consequence of this definition is that a section with a low level of particle velocity will easier exhibit a high relative error level. Fig. 3 shows the relative error levels in the measurement plane for the central area, for the edge and for the total area. For the central area the average relative error is seen to be lower than –18 dB over the entire calculated frequency range from 500 Hz to 5 kHz.

Fig. 4 shows the corresponding data for the calculation plane at $z = -3$ cm. Clearly, the error level has increased significantly, in particular along the edges, where the true particle velocity (z-component) is lower than before. The average error level over the central section/area is still better than around –18 dB up to 3.3 kHz and better than –12 dB up to 5 kHz.

Fig. 5 shows the Sound Power for the central and full sections of the calculation area at $z = -3$ cm. For both sections the sound power error is less than 0.2 dB up to

Fig. 3. Relative average error level for SONAH calculation of particle velocity in the measurement plane, z=0

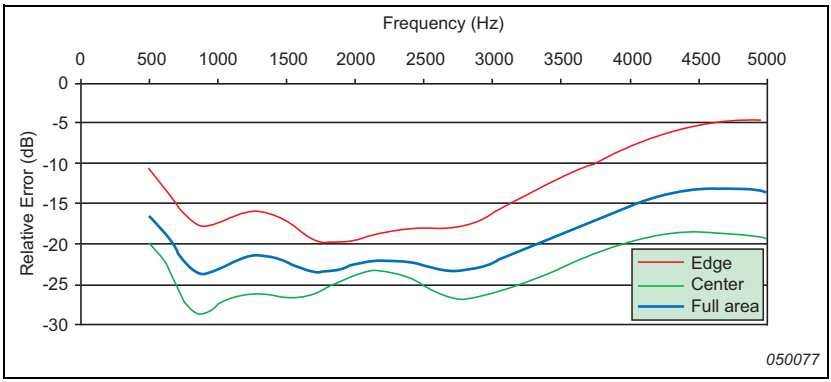

Fig. 4. Relative average error level for SONAH calculation of particle velocity in the calculation plane, z=–3 cm

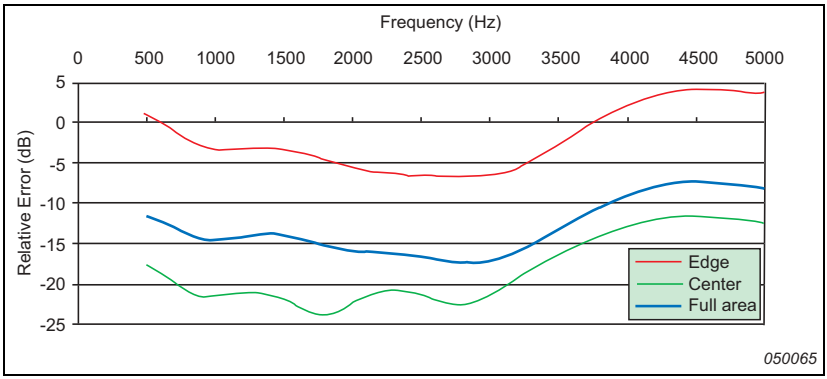

around 3.5 kHz. Above that frequency the estimated power slowly decreases, probably because the number of microphones is too small to uniquely determine general sound fields in that frequency range.

Practical Measurement

The SONAH calculation method has been implemented in Brüel & Kjær's Non-Stationary STSF software package, which is an implementation of Time Domain acoustical holography. Here, time histories of sound pressure must be measured

Fig. 5. True and estimated sound power for the central and the full sections of the calculation area at z = –3 cm

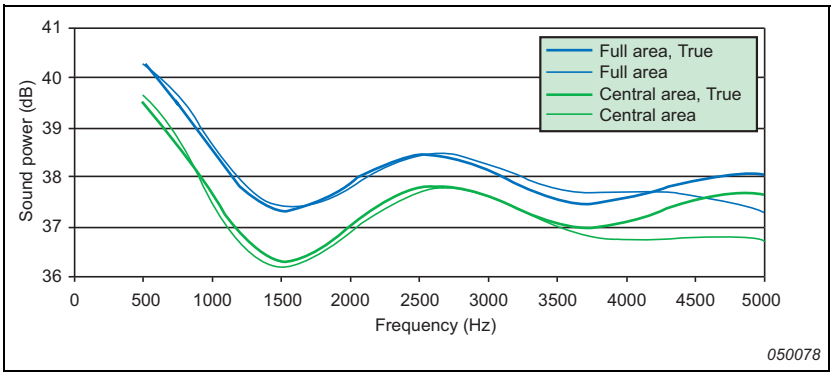

simultaneously at all measurement positions. The holography calculations are performed through an FFT transform of the full time-section to be studied to the frequency domain, followed by NAH or SONAH calculation for each FFT line and finally inverse FFT transform back to the time domain, [2]. In order to reduce the calculation time for the SONAH calculations, matrix interpolation was performed along the frequency axis on the correlation matrices $\mathbf{A}^{\dagger}\mathbf{A}$, $\mathbf{A}^{\dagger}\boldsymbol{\alpha}$ and $\mathbf{A}^{\dagger}\boldsymbol{\beta}$. With a few further efforts to reduce computation time, the SONAH calculations took only a few times longer than traditional NAH (based on spatial FFT processing) for the applied 120-element array.

The example to be presented here was a measurement on the side of the steel track of a large Caterpillar track-type tractor. The main sources of sound radiation were around the areas where the track passes over the sprocket and around the rear and front idlers. We took a measurement with a 10 cm spaced 10×12 element array positioned over a small Carrier Roller with a relatively low level of noise radiation. Fig. 6 shows a picture of the measurement area and plots of the A-weighted, time-averaged (RMS) particle velocity maps for the frequency band 205–1454 Hz (1/12 octave bands). Clearly, SONAH has a much better ability to suppress spatial window effects than the traditional NAH technique.

Fig. 6. Averaged Particle Velocity maps for the 1/12-octave bands 205–1454 Hz, A-weighted

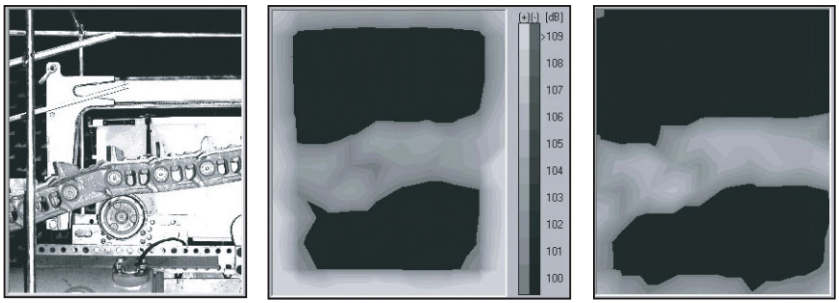

Conclusions

The new Statistically Optimal NAH (SONAH) method has been introduced. This method performs the plane-to-plane transformation directly in the spatial domain, avoiding the use of spatial FFT. Careful numerical programming ensures calculation times only slightly longer than FFT based NAH. Numerical simulations and practical results demonstrate that SONAH opens up a possibility to perform acoustical holography measurements with an array that is smaller than the source, and still keep errors at an acceptable level.

References

[1] Maynard J. D., Williams E. G., Lee Y., "*Near-field Acoustical Holography: I. Theory of Generalized Holography and the Development of NAH*", J. Acoust. Soc. Am. 78 (4), 1395–1413, October 1985.

[2] Hald J., "*Time Domain Acoustical Holography and Its Applications*", Sound & Vibration, 16–25, February 2001.

[3] Steiner R., Hald J., "*Near-field Acoustical Holography Without the Errors and Limitations Caused by the Use of Spatial DFT*", International Journal of Acoustics and Vibration, 6 (2), June 2001.

[4] Hald J., "*Planar Near-field Acoustical Holography with Arrays Smaller Than the Sound Source*", Proceedings of ICA 2001.

Previously issued numbers of Brüel & Kjær Technical Review

(Continued from cover page 2)

Special technical literature

Brüel & Kjær publishes a variety of technical literature which can be obtained from your local Brüel & Kjær representative.

The following literature is presently available:

- Catalogues (several languages)
- Product Data Sheets (English, German, French,)

Furthermore, back copies of the Technical Review can be supplied as listed above. Older issues may be obtained provided they are still in stock.

BV 0057 – 11 ISSN 0007–2621

HEADQUARTERS: DK-2850 Nærum · Denmark
Telephone: +45 45 80 05 00 · Fax: +45 45 80 14 05
www.bksv.com · info@bksv.com

Brüel & Kjær